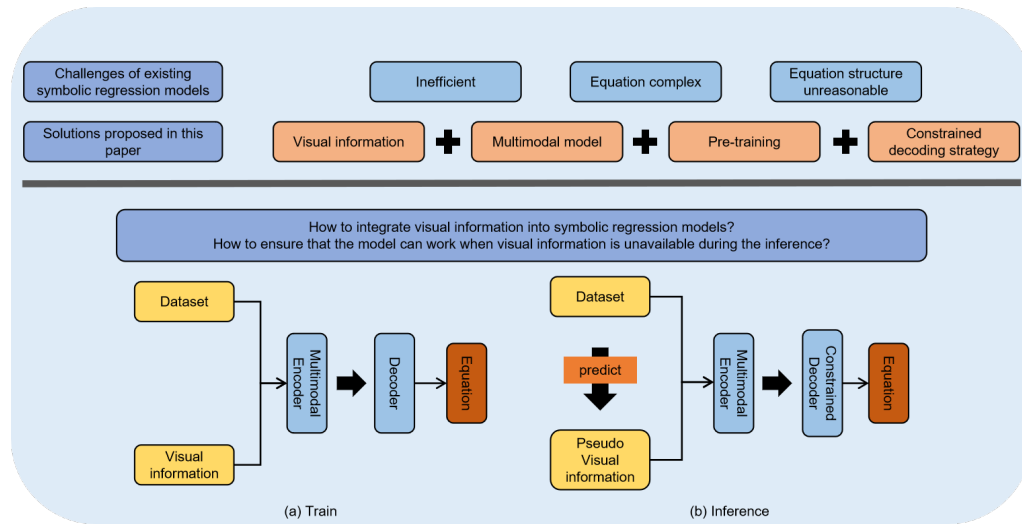


arXiv:2412.11139v1

Graphical Abstract

ViSymRe: Vision-guided Multimodal Symbolic Regression

Da Li, Junping Yin, Jin Xu, Xinxin Li, Juan Zhang



Highlights

ViSymRe: Vision-guided Multimodal Symbolic Regression

Da Li, Junping Yin, Jin Xu, Xinxin Li, Juan Zhang

- We propose a vision-guided multimodal symbolic regression model, called ViSymRe.
- We introduce a multivariable equation visualization method to support the training of the model.
- We propose dual-visual processing streams to enable the model to work when visual information is unavailable.
- Our model emphasizes the simplicity and structural rationality of the equations rather than merely numerical fitting.

ViSymRe: Vision-guided Multimodal Symbolic Regression

Da Li^{a,c}, Junping Yin^{c,d,f}, Jin Xu^{c,f}, Xinxin Li^{e,f}, Juan Zhang^{b,f,*}

^aAcademy for Advanced Interdisciplinary Studies, Northeast Normal University, Changchun, 130024, Jilin, China

^bInstitute of Artificial Intelligence, Beihang University, Beijing, 100191, Beijing, China

^cInstitute of Applied Physics and Computational Mathematics, Beijing, 100094, Beijing, China

^dNational Key Laboratory of Computational Physics, Beijing, 100088, Beijing, China

^eSchool of Mathematical Sciences, East China Normal University, Shanghai, 200241, Shanghai, China

^fShanghai Zhangjiang Institute of Mathematics, Shanghai, 201203, Shanghai, China

Abstract

Symbolic regression automatically searches for mathematical equations to reveal underlying mechanisms within datasets, offering enhanced interpretability compared to black box models. Traditionally, symbolic regression has been considered to be purely numeric-driven, with insufficient attention given to the potential contributions of visual information in augmenting this process. When dealing with high-dimensional and complex datasets, existing symbolic regression models are often inefficient and tend to generate overly complex equations, making subsequent mechanism analysis complicated. In this paper, we propose the vision-guided multimodal symbolic regression model, called ViSymRe, that systematically explores how visual information can improve various metrics of symbolic regression. Compared to traditional models, our proposed model has the following innovations: (1) It integrates three modalities: vision, symbol and numeric to enhance symbolic regression, enabling the model to benefit from the strengths of each modality; (2) It establishes a meta-learning framework that can learn from historical experiences to efficiently solve new symbolic regression problems; (3) It emphasizes the simplicity and structural rationality of the equations rather than merely numerical fitting. Extensive experiments show that our proposed model exhibits strong generalization capability and noise resistance. The equations it generates outperform state-of-the-art numeric-only baselines in terms of fitting effect, simplicity and structural accuracy, thus being able to facilitate accurate mechanism analysis and the development of theoretical models.

Keywords: Vision-guided symbolic regression, Multimodal learning, Mechanism analysis, Large model

1. Introduction

In 2009, Schmidt and Lipson published a groundbreaking paper in *Science*, demonstrating how symbolic regression could derive physical laws from experimental data Schmidt and Lipson

*Corresponding author at: Institute of Artificial Intelligence, Beihang University

Email address: dli@nenu.edu.cn (Da Li), yinjp829829@126.com (Junping Yin), xujin22@gscaep.ac.cn (Jin Xu), 51265500102@stu.ecnu.edu.cn (Xinxin Li), zhang_juan@buaa.edu.cn (Juan Zhang)

(2009). Their approach successfully discovered formulas in classical mechanics, such as the motion equations for pendulum systems and the laws of energy conservation, without any prior assumptions, highlighting the potential of symbolic regression in facilitating scientific discovery Wang et al. (2023); Krenn et al. (2022). As a machine learning method, symbolic regression aims to automatically discover mathematical or physical equations that best describe the relationships between variables (called independent variable, input variable, predictor variable and feature in different fields) and target (called dependent variable, output, response, outcome in different fields) from the given datasets. In fields like physics, chemistry, and ecology, symbolic regression is extensively used Quade et al. (2016); Neumann et al. (2020); Kim et al. (2020); Burlacu et al. (2023).

In the early 1990s, Koza introduced GP (Genetic programming) for symbolic regression, where individuals are regarded as equation trees with operators, variables and constants as nodes Koza (1993). GP simulates biological processes like gene replication, crossover and mutation to evolve individuals. When the initial population is large and the probabilities associated with crossover and mutation are well-calibrated, GP-based models show resistance to local optima. However, they typically converge slowly due to the large search space and often generate complex equations. Improvements, such as limiting the search space or modifying search strategies Schmidt and Lipson (2010); La Cava et al. (2016, 2018); Udrescu et al. (2020), have helped, but challenges remain. The main bottlenecks stem from the intensive call to the BFGS algorithm and the lack of directed search, prompting the development of GD (gradient descent) based and RL (reinforcement learning) based deep learning models Derner et al. (2018); Petersen et al. (2019); Mundhenk et al. (2021).

Recent advancement in symbolic regression is the introduction of pre-trained models Biggio et al. (2021); Valipour et al. (2021); Kamienny et al. (2022); Vastl et al. (2024); Liu et al. (2024); Li et al. (2024a); Merler et al. (2024); Li et al. (2024c,b), which learn the mapping between datasets—referred to as support point sets—and their corresponding equations. They undergo pre-training on millions of support point set-equation pairs, demonstrating excellent performance. Equation prediction can be completed with just a single forward pass, showcasing higher efficiency compared to GP-based and deep learning-based models, but at the cost of difficulty converging when the distribution of test points is previously unseen. To address this bottleneck, some rectification strategies to enhance the generalization capabilities of pre-trained models have been developed Landajuela et al. (2022); Shojaee et al. (2023); Liu et al. (2023). While these strategies have successfully expanded the application range of pre-trained models, they also introduce new challenges, such as lower computational efficiency and increased equation complexity, similar to issues encountered by GP and deep learning-based models.

Overall, existing symbolic regression models face challenges in balancing computational efficiency, fitting effect and the equation structure rationality, limiting their application to real-world problems. So, developing efficient models that can generate equations that are not only accurate but simple and consistent with the structure of basic physical equations is crucial for advancing symbolic regression technology and maximizing its practical applications across various fields.

Poincaré, in his work *Science and Hypothesis*, noted that mathematics is not only a logical deduction but also a construction based on “intuition” Poincaré et al. (2017) which often forms through rich experiences, aiding mathematicians in quickly finding effective solutions. Now, considering symbolic regression from the perspective of an experienced mathematician, when faced with a dataset (such as $\{-2, 4, [0, 0], [1, 1], \dots\}$ containing one variable and one target), what intuitions might emerge to facilitate equation prediction? The answer is none—this is

extremely challenging due to the abstract and unordered of dataset. However, if one sees a visual representation of this dataset showing a shape of parabolic, it is easy to associate it with power functions, thus significantly reducing the equation search space, see Fig. 1. This simple example demonstrates the positive roles that vision plays in symbolic regression. Similarly, pre-trained models, built upon extensive data training, possess a rich reservoir of knowledge. How to enable pre-trained models to generate human-like intuitions is essential to predicting equations quickly and accurately, the essence of which lies in the effective utilization of visual information from datasets.

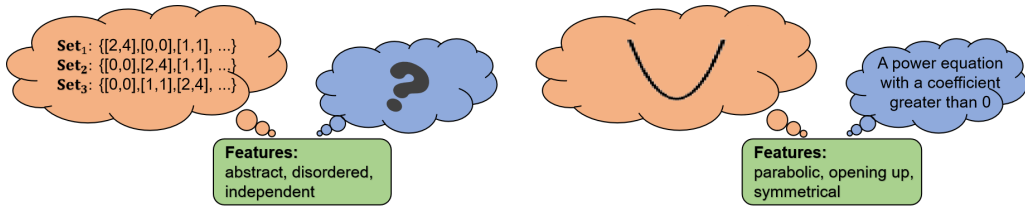


Figure 1: **Illustration of how visual information aids symbolic regression.** Visual features are specific, structured and clear, thereby facilitating the generation of intuitions.

In recent years, leveraging visual information to aid in solving complex machine learning tasks has demonstrated significant benefits, commonly used in language modeling Baltrušaitis et al. (2018); Liu et al. (2021); Li et al. (2023). They integrate visual information into a multimodal model to augment language understanding. Plausibility is obvious. For example, in the case of machine translation, despite originating from a distinct language, the English word “Dog” and the German word “Hund” share identical underlying visual perception. Multimodal technology has the potential to extend to symbolic regression, allowing the model to analyze typical patterns or shapes presented in the visualization of the dataset to select suitable base functions, thereby reducing the search space and improving accuracy.

Currently, visual symbolic regression is a novel approach that primarily faces challenges including the effective integration of three modalities: vision, symbol and numeric, the visualization of high-dimensional data and the absence of visual content during inference. Additionally, ensuring that the predicted equations are simple enough and well-structured also needs to be considered. In this paper, we introduce the first visual-guided model in the field (to the best of our knowledge) and provide reference solutions to these challenges. In competition with state-of-the-art symbolic regression models, our proposed model achieved the highest overall ranking, demonstrating its potential for widespread application in the fields of science and engineering.

Overall, our main contributions are as follows:

- We propose a vision-guided multimodal symbolic regression model that integrates visual information to enhance data analysis and symbolic learning, systematically exploring the promoting effects of vision on pre-trained model for fast and accurate equation prediction, transcending the traditional view of symbolic regression as a purely numeric-based regression technology.
- We introduce a dual-stream visual processing module (real and virtual), allowing our model to function even in the absence of visual input during inference. Experimentally validated, a well-trained virtual visual stream can not only accurately infer the visual features of equations from the given dataset, but also support the reconstruction of equation images.

- To extend our proposed model to multivariable scenarios and accelerate its convergence, we present an equation preprocessing method that enables the visualization of multivariable equations, allowing the model to observe how individual variables impact the target, thereby deepening the understanding of complex relationships within the equation.
- Our model emphasizes the simplicity and structural rationality of equations, rather than merely numerical fitting, providing richer and more accurate insights for mechanism analysis.

In Section 2, we introduce the related work. In Section 3, we detail the motivation and technical details of our work. In Section 4, we provide the comparison results between our model and the state-of-the-art baselines. Finally, the prospects and limitations of our work are discussed in Section 5.

2. Related work

GP-based models Classic symbolic regression models are achieved based on GP, which evolve equations through simulating natural selection and genetic mechanisms to optimally fit the given datasets Schmidt and Lipson (2009, 2010); McConaghy (2011); Arnaldo et al. (2014); La Cava et al. (2016); Virgolin et al. (2017, 2019); Udrescu et al. (2020); Burlacu et al. (2020); Cranmer (2023). GP-based models are effective in most scenarios, but their low computational efficiency hinders scalability to high-dimensional and large datasets, and they often generate complex equations.

Deep learning-based models Deep learning excels in extracting features from datasets, as detailed in prior studies Zhong et al. (2016). In the field of symbolic regression, deep learning is also widely applied. Sahoo et al. (2018) proposes a symbolic regression framework based on FNN (Feed-forward Neural Networks), where the activation functions are operators. This framework inherits the ability of deep learning to fit high-dimensional and nonlinear data, but the lack of a reasonable pruning strategy leads to often generating complex equations. Further, FNN is also employed in the preliminary stages of GP-based models, primarily for identifying simplified characteristics of the datasets, such as symmetry and parity Udrescu et al. (2020). In the study of Petersen et al. (2019), RNN (Recurrent Neural Networks) has been utilized to train the DSR (Deep Symbolic Regression) model. DSR treats the operators, variables and constants as tokens, and conceptualizes the symbolic regression as a process of token search. By restricting certain physically meaningless nesting of operators, the complexity of the equations generated by DSR is significantly lower than that of GP-based and other deep learning-based models. However, this comes at the cost of lower fitting effect and computational efficiency. Subsequently, GP and Monte Carlo search are integrated into the DSR framework Mundhenk et al. (2021); Xu et al. (2023b), which greatly improves the fitting effect.

Pre-trained models Recent researches have leveraged historical experience to accelerate symbolic regression, inspired by the success of Transformer-based models in various machine learning domains. Biggio et al. and Valipour et al. introduce the NeSymReS and SymbolicGPT respectively, which learn the mapping from support points to equation skeletons (with C as a constant placeholder) Biggio et al. (2021); Valipour et al. (2021), requiring little time to complete equation prediction. To further improve efficiency, Kamienny et al. propose an E2E (end-to-end) framework capable of predicting complete equations along with their constants, thereby eliminating the need to derive equation skeletons Kamienny et al. (2022). SNR uses a symbolic

network (SymNet) to represent equations and the encoding of SymNet provides supervision to train a policy network that can guide efficiently equation searches Liu et al. (2023). Overall, pre-trained models outperform GP and deep learning-based models in efficiency and can generate equations that follow a pre-designed “good” distribution by training on a well-crafted training set. However, pre-trained models are limited by their generalization capabilities, which might require larger training sets, broader support points sampling ranges, and enhanced architectural design.

Strategies for rectifying pre-trained models Recently, some rectification strategies have been proposed to address the challenge of pre-trained models being difficult to converge in unfamiliar domains. Landajuela et al. introduce a unified framework that uses initial inference results from a pre-trained model as priors for subsequent RL or GP steps Landajuela et al. (2022). Shojaee et al. employ the Monte Carlo search planning to guide the decoder of E2E Kamienny et al. (2022) model Shojaee et al. (2023). Liu et al. integrate the RL with a risk-seeking policy gradient into their proposed SNR framework Liu et al. (2023). These rectification strategies provide feedback on fitting losses and complexity, allowing dynamic adjustments to the pre-generated equation structures to enhance the generalization ability of pre-trained models. However, this comes at the cost of increased computational load and may lead to rectified equations that no longer follow to the pre-designed distribution of training equations, thereby facing new issues similar to those encountered by GP and deep learning-based models, such as increased equation complexity.

Multimodal models Early machine learning primarily focuses on single-modal learning, such as vision, text and audio Jordan and Mitchell (2015); Mahesh (2020); Surden (2021). The rise of deep learning has made the multimodal learning possible. Initially, multimodal learning focuses on how to transform different modalities into a unified feature representation. Classic methods usually use CNN to extract image features, RNN or LSTM to process sequence features, and then fuse them through FNN to obtain a multimodal representation Ngiam et al. (2011); Frome et al. (2013); Antol et al. (2015); Ramanishka et al. (2016). The introduction of contrastive learning methods allows the data of different modalities to be effectively aligned before fusing, thereby significantly improving the performance of multimodal models Gutmann and Hyvärinen (2010); Radford et al. (2021); Li et al. (2021); Jia et al. (2021). ViLBERT Lu et al. (2019) and LXMERT Tan and Bansal (2019) introduce the cross-modal attention mechanism, further enhancing the joint representation learning of visual and linguistic information. DALL-E Ramesh et al. (2021), Imagen Saharia et al. (2022) and Muse Chang et al. (2023) address challenges such as image quality and fine-grained control over generated content, representing significant advancements in generative modeling, and they have also achieved remarkable success in real-world applications. Recently, multimodal technology has also been introduced into symbolic regression. MMSR Li et al. (2025) considers the fusion representation of numeric and symbol, and introduces the contrastive learning and joint optimization strategies during the training process, achieving good fitting results. However, the potential impact of the visual modality is still not considered.

3. Method

Currently, the typically pre-trained symbolic regression models involve three steps:

- Deriving the order-invariant embedding for the input support points (encoding).
- Predicting the equation skeleton (decoding).
- Obtaining refined constants via the BFGS algorithm.

Achieving optimal performance relies on the judicious design of the encoder and decoder. In this section, we present the motivation behind our work and the key technical details of the proposed model. Overall, our model is composed of a multimodal encoder and a constrained decoder. Figs. 2 and 3 illustrate the training and inference processes of the model respectively. In the subsequent sections, we will provide a detailed discussion of each module, including their functions, design principles and key parameters.

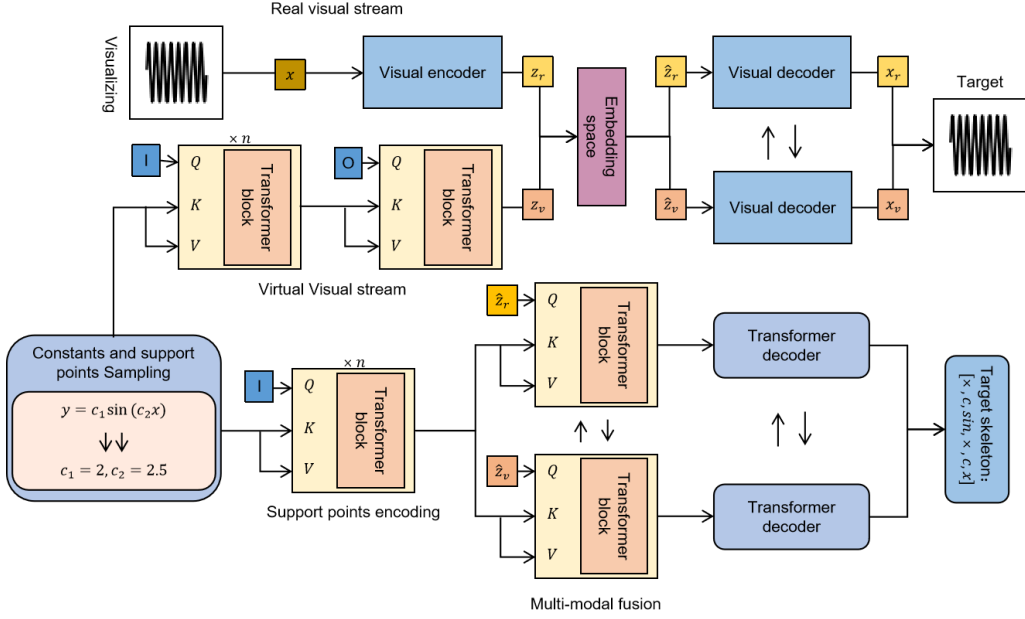


Figure 2: **The training pipeline of the proposed model.** It starts by sampling constants and support points from equation skeletons and performing visualization synchronously. The visual processing module includes two streams: the real (up) and the virtual (below), each of which contains an encoder and a shared (visual) decoder that constructs an auto-regressive pipeline, learning mappings from the equation images or support points to visual feature space and reconstructing the equation images. Subsequently, the visual features (real and virtual) and support point features are mapped into a unified space through a fusion module. Finally, the Transformer-decoder is used to predict the equation skeletons. To maintain consistency, the two visual streams share the same fusion module and Transformer-decoder.

3.1. Motivation

Existing symbolic regression models struggle to balance fitting effect, equation complexity and computational efficiency. Most of them prioritize fitting effect over simplicity, generating some well-fitting but extremely complex equations that reveal little about underlying physical mechanisms—contrary to the original purpose of symbolic regression.

Compared to GP and deep learning-based models, the pre-trained models have significant advantages in computational efficiency. More importantly, pre-trained models are better suited to integrate domain knowledge and other modalities to enhance the accuracy and structural rationality of the predicted equations, thus becoming a more promising approach Li et al. (2025).

Traditionally, symbolic regression has been regarded as a purely regression technique which implemented solely based on numeric, mainly because the GP-based models struggle to integrate other modalities into them. This limitation has acted as a technical bottleneck, severely restricting

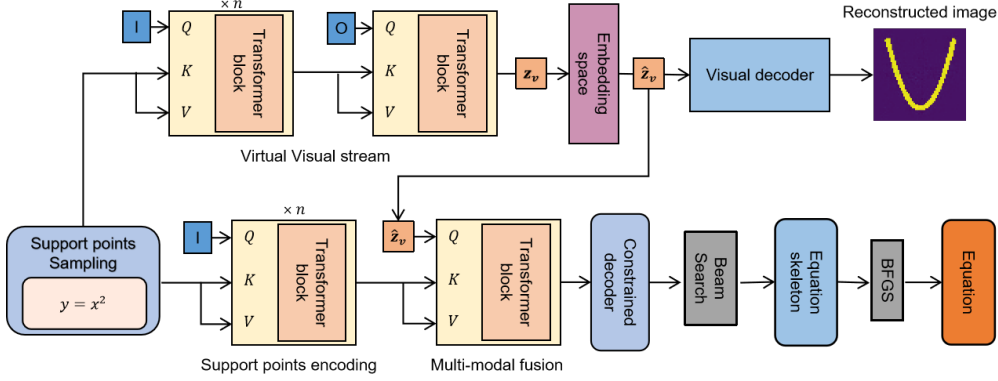


Figure 3: **The inference pipeline of the proposed model.** During the inference, the real visual stream is frozen since the real visual information is unavailable. The virtual visual stream predicts pseudo-visual features from support points, and then fused with the support point features to form multimodal representations. The decoding strategy is constrained to make the structure of the output equations reasonable. Beam search is used to improve the generalization of the decoder and BFGS is used to optimize the constants in the equation skeletons.

the evolution of symbolic regression models. In the Introduction 1, we have briefly discussed how visual information can enhance symbolic regression, and emphasized its advantages in guiding the model to develop human-like intuitions. At present, the success of large models, particularly large language models, in cross-modal learning, and the introduction of pre-trained models in symbolic regression, have provided both the motivation and technical support for achieving multimodal symbolic regression, making the integration of vision, symbol and numeric in a broad sense possible, despite the many challenges remain.

3.2. Multimodal encoder

The proposed multimodal encoder is divided into four parts. Their main functions are as follows:

- **Real visual stream:** Learning the visual features from equation images and reconstructing equation images through them.
- **Virtual visual stream:** Predicting pseudo-visual features from support points and reconstructing the equation images through them.
- **Support points encoding module:** Learning the features of support points.
- **Fusion module:** Fusing the support point features and visual (real or virtual) features into the multimodal representation.

3.2.1. Support points encoding

The input support point set is denoted as $D = \{(x_1, \dots, x_d, y_i)\}_{i=1}^n \in \mathbb{R}^{n \times (d+1)}$, where d and 1 represent the number of variables and target respectively, and n indicates the number of support points. Since the target may take extremely large or small values, leading to numerical instability, data normalization is necessary. However, commonly used methods, such as Min-Max and Z-score, destroy the internal structure of the support points, resulting in the predicted equation

being unable to represent the relationship of the original data. The E2E model solves this problem by remapping the variables in the predicted equation to the space before normalization, but this method makes the equation complicated Kamienny et al. (2022). Inspired by the work of Biggio et al. (2021), we adopted the IEEE-754 standard to transform the support points from float to multi-bit binary, which includes a 1-bit sign, 8-bit exponent and 10-bit mantissa. Thus, the shape of input support points becomes $R^{n \times ((d+1) \times 19)}$. Moreover, to avoid invalid values from operations such as dividing by 0 or taking the logarithm of a negative value and to maintain consistency in data format within the same batch, the points containing nan are set to 0.

We employ a multi-head attention module to achieve the encoding of support points, including 4 layers and 8 heads. Given that the computational complexity of the multi-head attention is proportional to the square of the number of support points (i.e. $O(n^2)$), we apply the inducing points (introduced by Set transformer Lee et al. (2019)) to reduce the computational burden, which is indicated by “I” in Figs 2 and 3. The inducing points form a trainable vector ($I \in \mathbb{R}^{(d \times 19) \times m}$, where $m \ll n$) that is used as the query vector in the multi-head attention module, achieving a low-dimensional mapping of the support points Lee et al. (2019). We fix m for each layer as a constant, $m = 100$.

3.2.2. Equation preprocessing for visualization

During training, the support points are randomly sampled, including ranges and values, which means that even for the same equation, the distribution of sampled support points may vary. So, to ensure consistent visual representation for the same equation, we opt to visualize the equation itself rather than the sampled support points. This approach is grounded in the fact that equations are known during training, there allowing them to be visualized synchronously. And by sampling points within the same range for visualizing, we guarantee consistency in the visual representation of each equation. When the equations are unknowable during the inference, the visual information is inferred from the support points, and the relevant technical details are discussed in Section 3.2.4.

Visualizing multivariable equations also poses challenges. Existing methods are primarily confined to three or lower dimensional data, such as curve and surface plots. A feasible approach is to fix the value of some variables at a constant (usually 1) while varying one variable at a time, thereby obtaining the curve that shows how this variable influences the target. However, this method is not without its flaws. For example, a special three-variables equation $f(x_1, x_2, x_3) = x_1(x_2 - x_3)$. When x_1 is the multiplication of the subtraction of the other two variables, $f(x_1, 1, 1)$ consistently equals 0, which means that no matter how x_1 changes, its impact on the target remains nil. In such cases, the relationship between x_1 and target cannot be captured through simple visualization. The lack of effective variation prevents the model from observing the potential effects of x_1 on target, resulting in the model incorrectly assuming that the variable x_1 does not exist. Without loss of generality, the problem equations that cannot be visualized by fixing variables also include dividing by 0 or performing logical operations with 0, such as $x_1/(x_2 - x_3)$ and $x_1 + \log(x_2 - x_3)$.

In addition, the impact of constants cannot be ignored. In the process of visualization by fixing variables, new constants are generated, which undergo complex operations with existing constants may result in an outcome that completely deviates from the original meaning of the equation. This in turn obscures the true behavior of the equation and potentially leads to misinterpretations of how variables influence each other. Furthermore, the visual consistency of the same equation cannot be guaranteed, as not only its support points but also the constants are randomly sampled during training to ensure the model’s generalization capability.

In this section, we introduce an equation preprocessing method to achieve the visualization of multivariable equations to assist in the training of our model. This method ensures that the equation images depict the relationships between a single variable and the target without interference from other variables. Additionally, our approach also aims to ensure that the visualization are not affected by constants, thereby maintaining consistency and avoiding extremely complex curve. Therefore, the visualization in fact targets the equation skeleton rather than the equation itself.

Algorithm 1 Pruning non-leaf nodes

```

1: Input:  $T$  : Original equation tree,  $X$  : Retention variable
2: Output:  $\hat{T}$  : Pruned equation tree
3: for node  $\in T$  do // Traverse all nodes
4:   if node  $\in$  Operator then
5:     if  $\nexists$  node.descendant  $\in [X, \pi, E]$  then // Determine if the sub-tree contains the
        specified elements
6:       node  $\leftarrow$  1 // Constant placeholder
7:        $T \leftarrow T \setminus$  node.descendant // Pruning
8:     end if
9:   end if
10: end for
11:  $\hat{T} \leftarrow T$ 
12: return  $\hat{T}$ 

```

To achieve the desired visualization, we define two equation preprocessing algorithms (Algorithm 1 and 2). They process equations in the form of the tree, focusing on the pruning of non-leaf nodes (operators) and leaf nodes (constants, variables) respectively. The specific steps are as follows:

- First, a retention variable is designated. Algorithm 1 traverses the equation tree and removes all sub-trees that do not contain the retention variable, π or e , thereby retaining only the parts related to the retention variable and special constants.
- Next, Algorithm 2 processes the remaining tree by replacing constants (excluding π and e) and non-retention variables with neutral elements: whose parent nodes are addition or subtraction are replaced with 0; whose parent nodes are multiplication or division are replaced with 1 or -1 depending on the sign. In this way, the equation is further simplified, containing only the necessary components related to the retention variable, π or e .

Consequently, the processed equation can be visualized as a two-dimensional curve that illustrates the relationship between the retention variable and target, unaffected by other variables and non-special constants. Fig. 4 demonstrates a process about how Algorithms 1 and 2 process the equation $x_1 + x_2 + x_1(x_2 - x_3)$ with x_1 designated as the retention variable. Detailed steps on how to visualize an equation containing d variables based on the proposed preprocessing method are provided in Appendix A.3.

3.2.3. Real visual stream

Existing visual processing technologies have matured significantly, such as ResNet He et al. (2016), GoogLeNet Szegedy et al. (2015) and ViT Alexey (2020). They excel at processing natural

Algorithm 2 Pruning leaf nodes

```
1: Input:  $T$  : Original equation tree,  $X$  : Retention variable
2: Output:  $\hat{T}$  : Pruned equation tree
3: for node  $\in T$  do // Traverse all nodes
4:   if node  $\in$  Constant or Variable and node  $\notin [X, \pi, e]$  then // Determine if the node is a
   non-reserved variable or constant
5:     if node.paraent  $\in$  [add,sub] then
6:       node  $\leftarrow$  0
7:     else if node.paraent  $\in$  [mul,div] then
8:       if node  $\in$  Constant and node  $<$  0 then // Keep the sign for multiplication and
       division.
9:         node  $\leftarrow$  -1
10:      else
11:        node  $\leftarrow$  1
12:      end if
13:    end if
14:  end if
15: end for
16:  $\hat{T} \leftarrow T$ 
17: return  $\hat{T}$ 
```

images in traditional visual tasks. However, equation images present some characteristics that are significantly different from natural images, such as regularity, symmetry, sparsity, geometric simplicity and low resolution, making some large visual processing models unsuitable for direct application in symbolic regression. In addition, after preprocessing (Section 3.2.2), an image often corresponds to multiple equations (for example, x^2 and $x^2 + c$ correspond to the same parabola), which makes it difficult to optimize the visual processing module only using the cross-entropy loss commonly employed in Transformer-based models.

Based on the discussion above, we adopt a generative encoder-decoder architecture as the real visual stream. Compared to using an encoder alone, the advantage of generative architecture lies in introducing a reconstruction loss to guide the module to train autoregressively, which enhances the quality of image encoding. Presently, most multimodal models consider continuous visual features, mainly due to the complexity and diversity of natural images. In this work, we consider the discrete visual embedding, because the preprocessed equations are represented as finite combinations of operators and retention variable, making their images finite in geometry, thus inherently discrete. Furthermore, discrete visual features have been proved easier to align with other modalities by DALL-E Ramesh et al. (2021).

The proposed framework stems from VQ-VAE Van Den Oord et al. (2017), a lightweight generative model that combines VAE and Vector Quantization (VQ) techniques. The working principle of VQ-VAE can be divided into three steps:

Encoding: The input data is first mapped into a continuous vector in the latent space through an encoder. This can be represented as:

$$\mathbf{z}_e = \text{Encoder}(\mathbf{x}), \quad (1)$$

where x represents the input data, and z_e is the continuous latent vector output by the encoder.

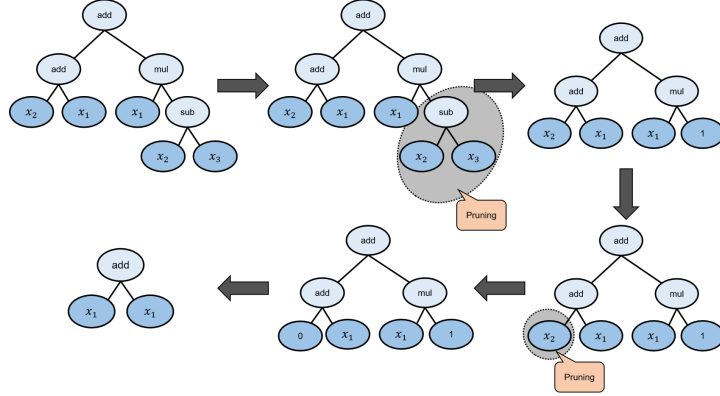


Figure 4: **An illustration of the preprocessing steps for a multivariable equation.** The original equation with three variables (x_1 , x_2 and x_3), and x_1 is designated as the retention variable. After preprocessing, a simple equation is obtained, retaining only the retention variable, depicting the independent relationship between this variable and the target.

Vector Quantization: A code book (embedding space) is defined, which contains a set of discrete vectors. The continuous latent vector z_e output by the encoder is then quantized by finding the closest vector in the code book based on similarity measures. This process can be formulated as:

$$\mathbf{z}_q = \arg \min_{\mathbf{e}_k \in E} \|\mathbf{z}_e - \mathbf{e}_k\|_2, \quad (2)$$

where z_q is the quantized vector, $E = \{e_1, e_2, \dots, e_K\}$ is the code book containing K discrete vectors, and $\|\cdot\|_2$ denotes the Euclidean distance.

Decoding: The quantized discrete vector z_q is then fed into a decoder to reconstruct the input data. This can be expressed as:

$$x_r = \text{Decoder}(\mathbf{z}_q), \quad (3)$$

where x_r represents the reconstructed input data.

We preserve the core structure of VQ-VAE yet redesign its encoder, decoder and embedding space to align with the dimensions of the input equation images. Specifically, we introduce an encoder consisting of three convolutional layers coupled with two down-sampling layers, transforming $64 \times 64 \times d$ input images into $8 \times 8 \times 512$. Embedding space has $K = 512$ vectors, each featuring 512 dimensions. The decoder is composed of three transposed convolutional layers, reconstructing the discrete features into a $64 \times 64 \times d$ image. In Fig 2, z_r is used to represent the continuous features, \hat{z}_r represents the quantized discrete features, and x_r represents the reconstructed image.

3.2.4. Virtual visual stream

The unavailability of visual information during the inference phase is the primary limitation of the generalization of our model, which stands in stark contrast to most multimodal tasks that rely on the immediate fusion of multi-source information. Fortunately, the visual information has been implicitly included in the support points. So, we propose a virtual visual stream, capable of generating pseudo-visual features based on the support points.

The core architecture of the virtual visual stream comprises an encoder and a decoder, analogous to that of the real visual stream. The encoder consists of 3 multi-head attention layers,

each with 8 heads. The input is the token sequences of support points, and the output is the pseudo-visual features. Distinct from the traditional stacking of multi-layer attention, we introduce a trainable vector (indicated by “ O ” in Figs 2 and 3) at the output layer, serving as a substitute for the query vector. It ensures that the output of the encoder of virtual visual stream can align with the $8 \times 8 \times 512$ -dimensional features outputted by the encoder of real visual stream.

Both the decoder and embedding space of the virtual visual stream are shared with those of the real visual stream, thereby establishing an auto-regressive pipeline. This signifies that a fully trained virtual visual stream can not only predict the visual features from support points but also reconstruct the original curves. In Figs 2 and 3, z_v , \hat{z}_v and x_v represent the continuous pseudo-visual features, the quantized discrete pseudo-visual features and the reconstructed image respectively.

3.2.5. Multimodal fusion

Currently, a series of intricate multimodal fusion modules have been proposed, tailored for diverse machine learning tasks such as machine translation Lin et al. (2020); Yin et al. (2020); Yao and Wan (2020); Li et al. (2022), sentiment analysis Gandhi et al. (2023); Zhu et al. (2023) and object recognition Lu et al. (2020); Yin et al. (2021). However, in the field of symbolic regression which involves the fusion of visual, symbol and numeric features, such research has not yet received sufficient attention. In Section 1, we have preliminarily discussed the analogy between symbolic regression and machine translation, as well as the similar roles played by visual information. In fact, a complete equation consists of several symbols (operators, constants and variables), just like a complete sentence consists of several words. Based on this fact, we establish a correspondence between the elements of symbolic regression and machine translation, where equations correspond to sentences and symbols correspond to words. Building on this concept, we envision extending multimodal techniques from image-sentence pairs to image-equation skeleton-support point set pairs.

Zhang et al. introduced a Transformer-based multimodal machine translation model Zhang et al. (2020) that can provide some inspiration. Their approach involves establishing a topic-image lookup table, where a topic consists of one or a few words, and an image is a visual representation of the topic, see in Fig. 5a. In this lookup table, a topic corresponds to multiple images, and an image may also correspond to multiple topics. By retrieving from the lookup table, a sentence and its corresponding set of images are obtained. When calculating attention, the sentence is used as the query vector, and its corresponding images are used as the key and value vector.

A similar fusion approach can be adapted for our model. However, an image can correspond to multiple equation skeletons, with each skeleton further associated with different support point sets. Therefore, the image-equation skeleton pairs and the equation skeleton-support point set pairs present a one-to-many relationship, whereas a support point set corresponds to only one image, as illustrated in Fig. 5b.

Based on the above discussion, we propose an attention-based fusion module with 4 layers and 8 heads. The visual features are used as the query vector, while the features of support points serve as key and value vectors. Notably, the visualization process is CPU-intensive, leading to significant computing consumption during the model training. Inspired by the work of Zhang et al. Zhang et al. (2020), we establish an image-equation skeleton lookup table to avoid repetitive visualization of the same skeleton, the details of which are provided in Appendix A.4.

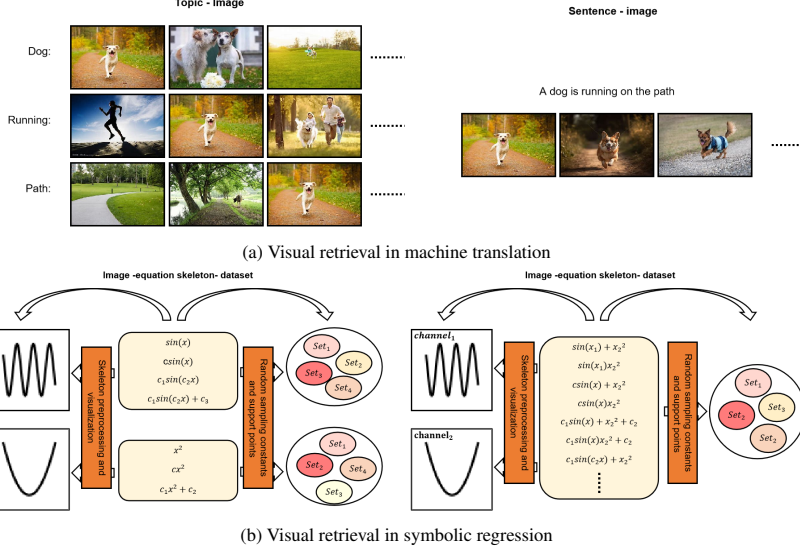


Figure 5: **Illustration of the visual retrieval in machine translation (a) and symbolic regression (b).** In (b), the left are two univariable examples, and the right is a multivariable example. Each image corresponds to multiple skeletons and thus to multiple support point sets which are infinite due to the randomness of the constants in skeletons and the randomness of sampling points.

3.3. Multimodal alignment

Before multimodal fusion, aligning different modalities is necessary Shen et al. (2023); Han et al. (2024). Due to inherent differences in data characteristics among modalities, direct fusion without alignment can lead to information confusion, thus degrading the performance of multimodal models. To address this issue, we introduce contrastive learning to align the support point features and visual features before fusion Gutmann and Hyvärinen (2010); Li et al. (2021). The contrastive learning loss function is as follows:

$$\mathcal{L}_{CL} = -\frac{1}{M} \sum_{i=1}^M \log \left(\frac{\exp(s_i^T v_{i_+} / \tau)}{\sum_{j=1}^N \exp(s_i^T v_j / \tau)} \right) - \frac{1}{N} \sum_{i=1}^N \log \left(\frac{\sum_{k \in K_{i_+}} \exp(v_i^T s_k / \tau)}{\sum_{j=1}^M \exp(v_i^T s_j / \tau)} \right), \quad (4)$$

where s_i represents the feature vector of the i -th support point set, v_{i_+} denotes the feature vector of the visual input that corresponds to s_i , v_i represents the feature vector of the i -th visual input, K_{i_+} is the set of the feature vectors of support point sets corresponded with v_i , M is the total number of support point sets in the batch, N is the total number of visual inputs in the batch, and τ is a temperature parameter.

Before calculating the \mathcal{L}_{CL} , the support point features and visual features are first mapped to a unified space, making them comparable in the same dimension. By minimizing the \mathcal{L}_{CL} for multiple pairs of support point sets and visual inputs in a batch, the model aims to maximize the similarity between positive samples (support point sets and visual inputs that correspond to each

other) while minimizing the similarity between negative samples (support point sets and visual inputs that do not correspond). Specially, since each visual input may correspond to multiple support point sets, repeated visual inputs in the batch will be deleted, i.e., $N \leq M$.

3.4. Decoder

We utilize the Transformer-decoder with 8 layers and 8 heads to achieve the equation decoding. The output is structured to follow the pre-order traversal of the equation tree, ensuring that the predicted equations remain logically and mathematically valid.

We recognize that adhering to physical laws imposes constraints on the structure of equations. Not all equations are meaningful or valid. For instance, simple structures like $\cos(\sin(x))$ or more complex structures like $\exp^{\log(\cos(x))}$ often don't correspond to any physical law Petersen et al. (2019). We develop a constraint strategy that functions by actively monitoring the ancestor nodes of the current position during the decoding process, to adjust the probability of outputting certain symbols, thereby constraining the structure of the equation. The presence of risky operators (such as exponential functions and trigonometric functions) at the ancestor nodes is a key indicator that an irrational nesting might occur in subsequent steps. As a constraint, if any suspicious ancestor nodes are detected during decoding, the probability of outputting symbols that might lead to unreasonable nesting will be set to 0.

Since the number of support points sampled for each equation is limited during training, the performance of the model may descend when the number of test points significantly exceeds this threshold. According to the experience of Kamienny et al. (2022), we select B bags, each of which is a random subset of the test points. For each bag, we apply beam search to generate C candidate equation skeletons. The optimal skeleton is determined as the prediction results through the fitting loss and penalty of $1e-14$ per token. Then, we use the BFGS algorithm to optimize the constants within it, which is a standard choice, though other feasible algorithms can be considered (such as L-BFGS, Davidon-Fletcher-Powell and some gradient-based optimization algorithms), especially when the precision or efficiency is not meet the requirements Biggio et al. (2021); Valipour et al. (2021). Finally, the model re-evaluates the optimized equations by removing the terms with extremely small coefficients, as these may represent potential noise. Typically, the threshold is set at $1e-5$.

3.5. Optimization

We propose a joint optimization strategy to train our model, allowing all modules to converge simultaneously. For the real visual stream, the loss is defined as:

$$\mathcal{L}_R = \|x - z_r\|_2 + \|e - \text{sg}[\hat{z}_r]\|_2 + \beta \|\text{sg}[e] - \hat{z}_r\|_2, \quad (5)$$

where x represents the real equation image, x_r is the reconstruction of whose. \hat{z}_r is the quantized vector, e is the code book in discrete embedding space and β (by default, $\beta = 0.2$) is a hyperparameter. $\text{sg}[*]$ is an operator, indicating to stop gradient. The first term is reconstruction loss, which measures the discrepancy between the reconstructed image x_r and the real image x . The second term is vector quantization loss. Since the mapping from z_r to \hat{z}_r uses a straight-through gradient estimation, the embedding e does not directly receive gradients from the reconstruction loss. Therefore, to learn a meaningful embedding space, the vector quantization loss is introduced. The third item is commitment loss, which constrains the output of the encoder to be consistent with the embedding space.

For the virtual visual stream, the loss is defined as:

$$\begin{aligned} \mathcal{L}_V = & \|x - x_v\|_2 + \|z_v - z_r\|_2 \\ & + \|e - \text{sg}[\hat{z}_v]\|_2 + \beta \|\text{sg}[e] - \hat{z}_v\|_2, \end{aligned} \quad (6)$$

which is similar to that of the real visual stream. In order to make the output of the real visual stream and the virtual visual stream meet the desired consistency, we add an additional loss term $\|z_v - z_r\|_2$.

The overall skeleton prediction loss is described as:

$$\mathcal{L}_E = \mathcal{L}_{E_r} + \mathcal{L}_{E_v}, \quad (7)$$

where \mathcal{L}_{E_r} and \mathcal{L}_{E_v} are cross-entropy loss, representing the skeleton prediction losses of the real visual stream and the virtual visual stream respectively.

Although the virtual visual stream can be trained independently, there might still be a gap in the level of training compared to the real visual stream, as reflected in the inconsistency of the predicted equation skeletons. To enhance their consistency, we use KL divergence to define a consistency loss \mathcal{L}_C .

Overall, the optimization objective of the proposed model is the weighted sum of real visual loss \mathcal{L}_R , virtual visual loss \mathcal{L}_V , skeleton prediction loss \mathcal{L}_E , consistency loss \mathcal{L}_C and contrastive learning loss \mathcal{L}_{CL} (Eq. 4):

$$\mathcal{L} = \alpha(\mathcal{L}_R + \mathcal{L}_V) + \mathcal{L}_E + \mathcal{L}_C + \mathcal{L}_{CL}. \quad (8)$$

α is an empirical parameter used to balance the weight of partial losses, which is set to 0.1.

4. Experimental results

In this section, we provide a comprehensive evaluation of the proposed model’s performance. The method for generating the data required for the evaluations is provided in Appendix A. We divide the experiments into in-domain and out-of-domain. In the in-domain experiments, we select classic pre-trained models to compare with the proposed model under the same training conditions, while the out-of-domain experiments involve more extensive evaluations related to GP-based and deep learning-based models. In the remainder of this paper, we will use the name “ViSymRe” to refer to the proposed model.

4.1. Metrics

In our experiments, there are four metrics to evaluate the models’ performance:

- **R^2 -score:** R^2 -score measures how well the predicted equation fits the data. The closer the value of R^2 -score is to 1, the better the predicted equation fits the data. Its formula is described as:

$$R^2 = 1 - \frac{\sum_{i=1}^n (y_i - \hat{y}_i)^2}{\sum_{i=1}^n (y_i - \bar{y})^2},$$

where y_i represents the observed values, \hat{y}_i represents the predicted values and \bar{y} is the mean of the observed values. If $R^2 \geq 0.99$, the equation is considered to be correctly predicted.

- **R^2 acc:** R^2 accuracy represents the proportion of equations that can accurately predict to the total test equations.
- **Complexity:** Complexity is considered as the number of symbols in equations. If a predicted equation fits the dataset well and is simple, it is considered to be a good equation.
- **Symbolic solution rate:** Symbolic solution is intended to identify the predicted equations that differ from the true equations by a constant or scalar amount. It is first introduced by La Cava et al. (2021), and defined as follow:

Definition 1. An predicted equation \hat{f} considered ad a symbolic solution to a problem with the ground-truth equation $f + \epsilon$, if \hat{f} does not simplify to a constant, and at least one of the following conditions holds true:

- $f = \hat{f} + \alpha$, where α is constant;
- $f = \hat{f}/\beta$, where β is constant and $\beta \neq 0$.

Before evaluating the symbolic solution, each equation is simplified using SymPy Meurer et al. (2017). Compared to traditional metrics like R^2 -score, which focus on numerical accuracy, symbolic solution provides a deeper assessment of a model’s ability to capture the true equation structure La Cava et al. (2021). However, since the same equation can be represented in multiple structures and the simplifying by SymPy may not be optimal, it cannot guarantee the perfect identification of all symbolic solutions.

The symbolic solution rate is defined as the proportion of the equations that can accurately identify symbolic solutions to the total test equations.

4.2. In-domain experiments

NeSymReS Biggio et al. (2021) and SymbolicGPT Valipour et al. (2021) are both the pre-trained equation skeleton prediction model. We selecte them as the baselines for our in-domain experiments. Note that the original symbolicGPT uses “text” to represent the equation skeleton (e.g., the equation $\sin(x)$ is represented as $\{ 's', 'i', 'n', '(', 'x', ') ' \}$) instead of the tree structure, which is not conducive to the unification of training scenarios, so we modified it. All models are pre-trained on the same training set containing randomly generated 1 million equation skeletons, each with up to 3 variables, over a period of 10 epochs. To ensure fairness, all experiments are repeated 10 times.

We first evaluate the test models on 1000 randomly generated equations. To minimize the influence of the BFGS algorithm on the final results and to capture symbolic solutions as accurately as possible, all test equations are designed without constants. Details of other parameters employed in testing are provided in Table 1. In this experiment, we particularly focus on how the proposed decoder constraint strategy enhances various metrics of ViSymRe. The test results as shown in Fig. 6, reveal that ViSymRe achieves significantly higher R^2 accuracy and symbolic solution rate compared to NeSymReS and SymbolicGPT. Notably, the ViSymRe with the constrained decoder improves the symbolic solution rate, although there is a slight decrease in R^2 accuracy, highlighting the positive impact of the proposed constraint strategy in enhancing the structural rationality of the predicted equation. Moreover, the results of 10 times experiments of the ViSymRe with the constrained decoder demonstrate notable consistency, particularly in symbolic solution rate,

Table 1: The default parameters employed in testing.

Description	Value
Number of support points	500
Number of bags	10
Number of support points per bag	200
Beam size	10
Noise level	0
Sampling range of support points	$\mathcal{U}(-10, 10)$
Initial value sampling range of constant for BFGS	$\mathcal{U}(0, 10)$
Number of BFGS restarts	10

demonstrating an unexpected effect of the constraint strategy in enhancing the stability of the ViSymRe.

Fig. 7 illustrates the average time required by each model to complete the prediction of an equation. It is observed that, despite ViSymRe with the constrained decoder being architecturally more complex than the others, it requires the least computing time. This efficiency is attributed to its ability to identify simple and well-structured equations, significantly reducing the computational overhead associated with beam search and BFGS optimization, which are the primary burdens of pre-trained models.

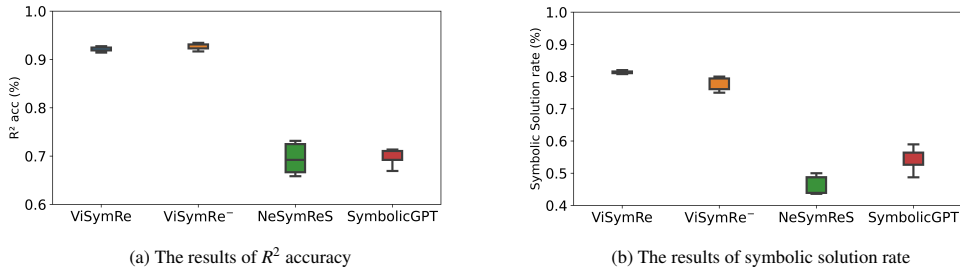


Figure 6: Test results of ViSymRe (with constrained decoder), ViSymRe⁻ (with Transformer decoder), NeSymReS and SymbolicGPT on 1000 randomly generated equations that do not contain constants.

We conduct a series of ablation experiments on 1000 randomly generated equations to assess the sensitivity of ViSymRe and baselines to various factors, including noise levels, the number of constants, the number of test points, the number of unary operators, the distributions of support points and beam size. In testing, except for the ablation factors and randomly adding no more than 3 constants to each equation, other parameters use the default values in Table 1. We report the average results across various experimental scenarios from 10 experiments in Fig. 8. As the difficulty factors increase, the performance of all models declines, which is a predictable outcome.

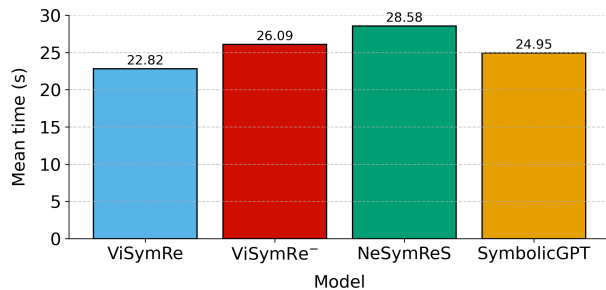


Figure 7: Mean prediction time of ViSymRe, ViSymRe⁻, NeSymReS and SymbolicGPT.

However, compared to baselines, ViSymRe exhibits the best robustness across all scenarios, demonstrating its ability to accurately predict equations with varying difficulties.

4.3. Out-of-domain experiments

In out-of-domain experiments, we evaluate ViSymRe on several databases released by SR-Bench La Cava et al. (2021), including 119 Feynman Udrescu et al. (2020) problems, 14 ODE-Strogatz Strogatz (2018) problems and 122 black box regression problems with unknown underlying equations. In addition, a new challenging benchmark SRSD-Feynman has been published recently, which resamples the 119 Feynman problems in a new range Matsubara et al. (2022). The details of the used databases are described in Appendix C.

The sample points for each problem are randomly split into 75% training and 25% testing. Specially, for SRSD-Feynman problems, we use the training and test set divided by the publisher. For black box regression problems, we only use the instances with continuous features and less than 10 dimensions, because the pre-trained ViSymRe and E2E support a maximum of 10 input variables.

ViSymRe is trained on a training set containing randomly generated 5 million equation skeletons with up to 10 variables. The Adam optimizer is used to minimize the loss, and the learning rate is adjusted using cosine annealing strategy. For the other parameters of ViSymRe used in testing, including the number of bags, the number of test points per bag, beam size and BFGS-related parameters, see Table 1. We compare ViSymRe with state-of-the-art symbolic regression models, including Schmidt and Lipson (2010); McConaghy (2011); Arnaldo et al. (2014); La Cava et al. (2016); Virgolin et al. (2017); Cava et al. (2018); Jin et al. (2019); Petersen et al. (2019); Virgolin et al. (2019); Udrescu et al. (2020); Burlacu et al. (2020); de Franca and Aldeia (2021); Kamienny et al. (2022); Landajuela et al. (2022); Cranmer (2023); Shojaee et al. (2024), the results of which are referenced from La Cava et al. (2021); Matsubara et al. (2022); Kamienny et al. (2022); Shojaee et al. (2024).

For the benchmark of 119 Feynman problems, we evaluate symbolic regression models in terms of R^2 accuracy and equation complexity. Fig. 9 presents the results. We can see that ViSymRe achieves the best overall performance. Unlike purely numeric-driven models that are easy to overfit or generate overly complex equations, the equations predicted by ViSymRe are not only accurate but also simple. Since the Feynman problems approximate the distribution of natural laws observed in the real-world, strong performance on this benchmark indicates that ViSymRe has the potential to reveal interpretable equations from observational or experimental data.

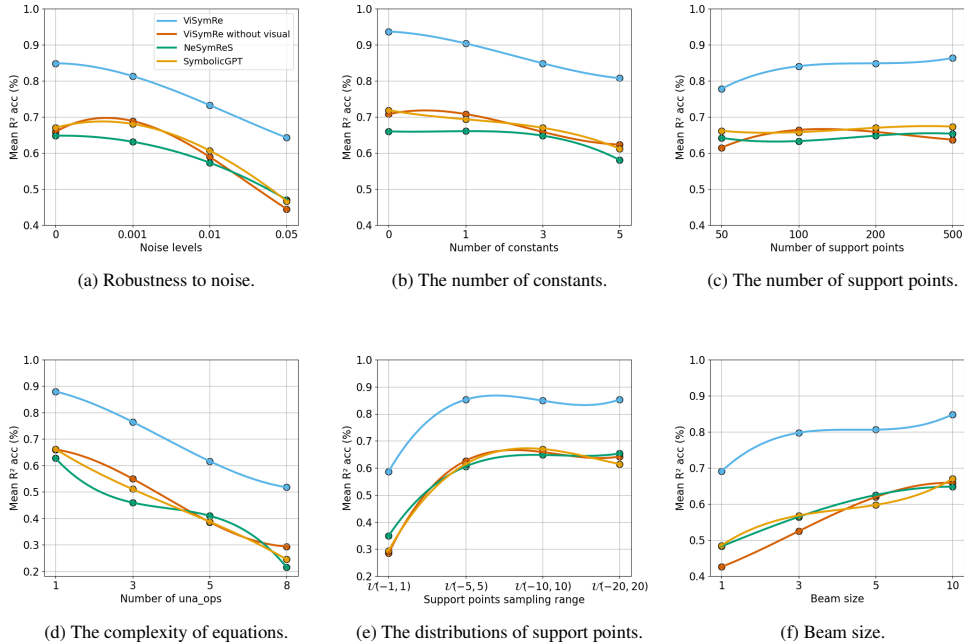


Figure 8: **Ablation experiment results.** Each subfigure shows the ablation of one factor.

The ODE-Strogatz database poses a challenge to the generalization capabilities of pre-trained models, as the data points exhibit a distinct temporal order, unlike the Uniform and Gaussian distribution encountered during the training phase of ViSymRe and E2E. Fig. 10 reports the mean R^2 results. Unsurprisingly, the ranking of E2E shows a notable decline compared to that of the Feynman problems. However, ViSymRe still maintains the best balance of fitting effect and complexity, primarily due to the enhancing effect of the visual modality on model training.

Fig. 11 summarizes the results of symbolic solution rate on Feynman and ODE-Strogatz problems. We observe a significant improvement in the ranking of the AIFeynman model in the symbolic solution evaluation compared to its ranking in the R^2 evaluation, particularly when targeting low noise scenarios, which highlights its advantage in discovering real physical equations. However, AIFeynman struggles to maintain this advantage when the noise level exceeds 0.01. In contrast, ViSymRe demonstrates strong robustness across various noise levels. For Feynman problems, the symbolic solution rate of ViSymRe is 2-3 times higher than any other models except AIFeynman. Notably, even at the noise level of 0.1, ViSymRe’s symbolic solution rate still exceeds that of other models at the noise level of 0, with the exception of AIFeynman. On the ODE-Strogatz dataset, ViSymRe maintains a consistent symbolic solution rate across noise levels of 0, 0.01 and 0.1, leading all other models except GP-GOMEA and AIFeynman. However, the latter two are particularly sensitive to noise, especially when noise exceeds 0.01, where their symbolic solution rates approach 0%. Overall, ViSymRe maintains a leading position in comprehensive symbolic solution rates across different datasets and noise levels, being consistent with our initial goal for it to discover equations that not only fit data well but are also simple and structurally accurate.

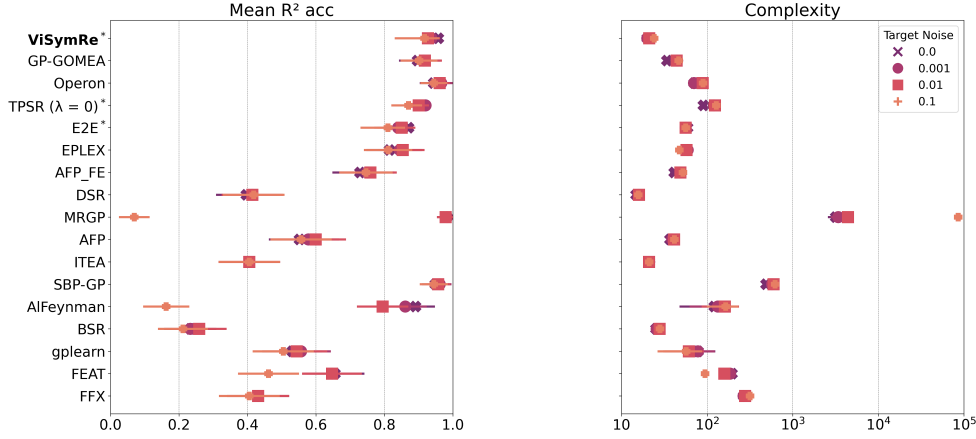


Figure 9: The average results on 119 Feynman problems, for 10 random seeds and subjected to three levels of target noise. Models are ranked based on their combined performance of R^2 accuracy and complexity overall target noises. The ones marked with * are pre-trained models.

We use the median R^2 to assess the fitting effect of the tested models on black box problems, because median is less sensitive to outliers than mean, enabling a more robust evaluation. Fig. 12 reports the results, with models positioned closer to the bottom-right corner exhibiting more advanced performance. Since the underlying equations of black box problems may not conform to the distribution or structure of real physical equations, it is difficult for ViSymRe to find equations that fit data well and are well-structured for these problems. The same challenge is encountered by AIFeynman. As a result, the median R^2 of ViSymRe and AIFeynman are lower than that of the state-of-the-art symbolic regression models which improve the R^2 by increasing the complexity and structural flexibility of the predicted equations. But overall, advanced symbolic regression models including ViSymRe have achieved higher fitting effect and lower complexity than classical regression models, indicating that symbolic regression, as an interpretable modeling tool, can effectively solve practical problems in the real world.

The 120 problems in SRSD-Feynman are divided into three clusters based on their difficulty: easy, medium and hard, containing 30, 40 and 50 problems respectively. We compared ViSymRe to the baselines reported by Matsubara et al. (2022). The results of easy, medium and hard problems are outlined in Table 2. Observation shows that ViSymRe still leads pre-trained model E2E and most GP-based models. On easy problems, ViSymRe performs very well, obtaining second place. However, on medium and hard problems, ViSymRe falls slightly short of the state-of-the-art models, which is primarily due to the difference in the training distribution of ViSymRe and the sampling distribution of SRSD-Feynman. The support points of ViSymRe during training are primarily concentrated in a Uniform distribution ranging from $[-20, 20]$, whereas SRSD-Feynman uses a log-uniform distribution that can reach values as high as $1e30$. Another factor reason for the performance decline of ViSymRe is the optimization strategy of BFGS, where initial constant values are randomly sampled from $[0, 10]$, which is vastly different from the distribution of constants in SRSD-Feynman (reaching up to $1e8$). However, experience shows that this issue can be effectively improved by expert-provided priors. On the whole, not

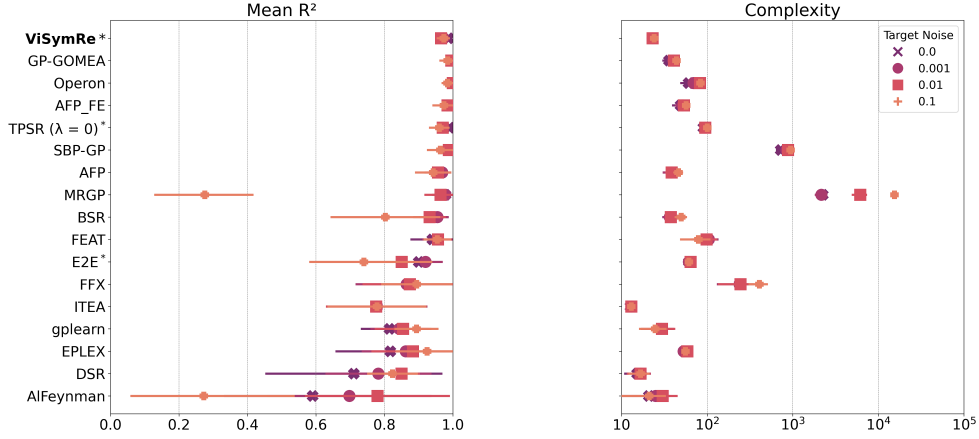


Figure 10: The results on 14 ODE-Strogatz problems.

just ViSymRe, but most GP and deep learning-based models also struggle with SRSD-Feynman problems, with R^2 accuracy often in the single digits. This suggests that complex data distributions pose significant challenges not only for pre-trained models but also GP and deep learning-based models.

Table 2: The results of ViSymRe and baselines on SRSD-Feynman problems.

Metric	Group	SRSD-Feynman								
		gplearn	AFP	AFP-FE	AIF	DSR	E2E	ViSymRe	uDSR	PySR
Accuracy ($R^2 > 0.999$)	Easy	6.67%	20.00%	26.70%	33.30%	63.30%	26.70%	66.70%	100%	66.70%
	Medium	7.50%	2.50%	2.50%	5.00%	45.00%	17.50%	37.50%	75.00%	45.00%
	Hard	2.00%	4.00%	4.00%	6.00%	28.00%	14.00%	16.00%	20.00%	38.00%

5. Conclusions

In recent years, the successful application of AI (Artificial Intelligence) for science has reignited interest in symbolic regression. As a tool for scientific modeling, symbolic regression is no longer a simple numerical fitting but should encompass a comprehensive consideration of model efficiency as well as the simplicity and structural rationality of the output equations. However, existing technologies still face challenges in balancing these requirements. In this paper, we propose a vision-guided multimodal model, called ViSymRe, to introduce visual information into symbolic regression and explore its positive role in solving various symbolic regression challenges. To extend ViSymRe to multivariable scenarios and ensure its availability in the absence of visual input, we innovatively propose an equation preprocessing method and a dual-visual-stream design. A series of ablation and sensitivity evaluations show that ViSymRe has strong generalization

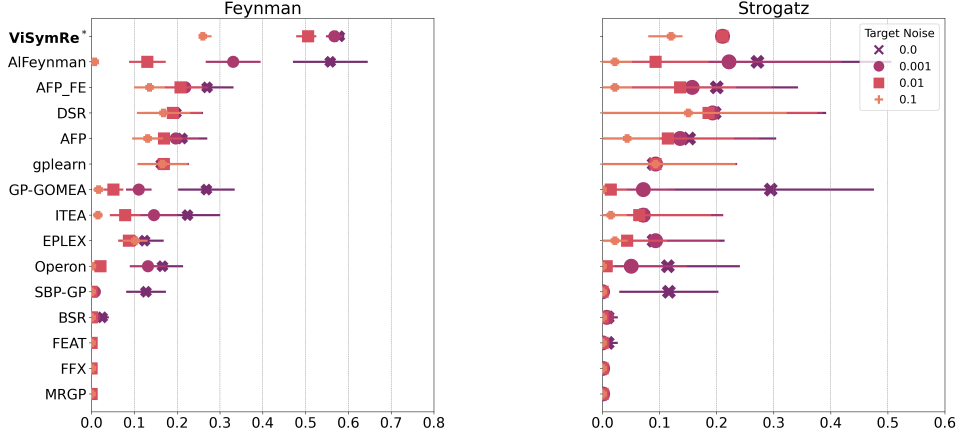


Figure 11: Symbolic solution rates on Feynman and ODE-Strogatz problems.

capabilities across various scenarios, exhibiting the most balanced performance across multiple metrics, including R^2 , complexity, symbolic solution rate and noise resistance, which highlights its potential as a valuable tool to promote scientific discovery.

Limitations Currently, pre-trained symbolic regression models remain an emerging method, though encouraging results have been achieved. A major limitation lies in how to train these models on more complex support point distributions, or how to generalize trained models to unseen distributions with minimal or no loss in performance. Although ViSymRe has shown that expanding the training set or exploring more suitable encoder and decoder can significantly ameliorate this problem, challenges remain. In fact, limited generalization capacity is a primary constraint in expanding the pre-trained models in any field, not just symbolic regression.

Future work Overly complex support point distributions can cause ViSymRe to fail to converge, even after normalization, such as the log-uniform distribution provided by SRSD-Feynman problems. This is a direct reason why pre-trained models like ViSymRe and E2E struggle to effectively solve SRSD-Feynman challenges. Some rectification strategies that are based on the GP and RL provide a technical approach to expand the application of pre-trained models to wider data distributions Shojaei et al. (2024); Landajuela et al. (2022); Liu et al. (2023). However, increasing computational time or generating “suboptimal” equation structures to obtain better fitting results may be costly, as discussed in Section 2.

Furthermore, we note that physical problem modeling also imposes requirements on the dimensional consistency of the equations. In fact, the decoding constraint strategy of ViSymRe has the potential to capture more information about the ancestor nodes of the current position, such as units and symbol frequency, which can further constrain the equation structure to satisfy dimensional constraints. We are building a library containing dimensions and their conversion relationships, and it will take time to ensure the authority. This work will be presented in the future.

Overall, future work for us will build on ViSymRe to explore more optimal combinations of pre-trained models with GP or RL, aiming to develop a general model that is computationally

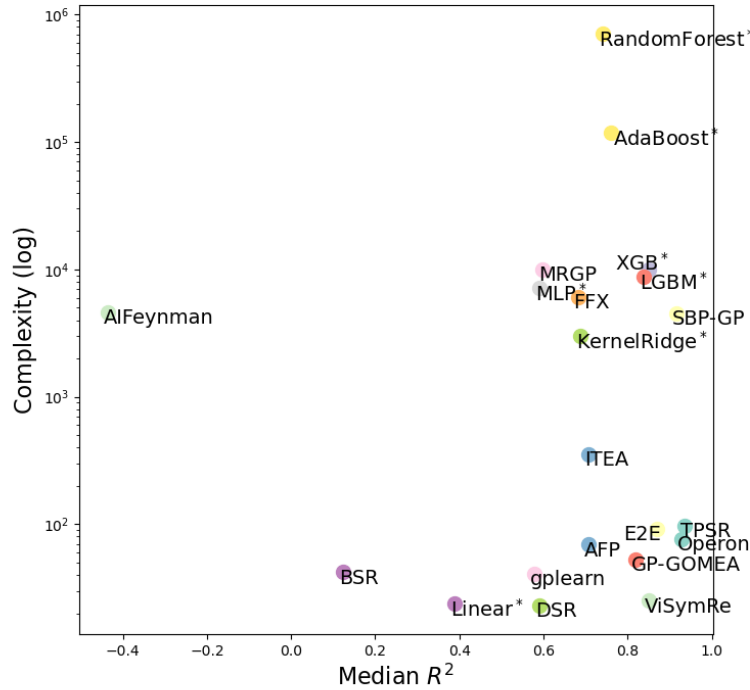


Figure 12: The results on black box problems. Models marked with * are classic regression models.

efficient and capable of generating well-fitted, simple and physically reasonable equations.

Potential positive impacts ViSymRe has achieved the best symbolic solution rate and the best balance between fitting effect and equation complexity, which means it holds the potential to be an effective tool not only in symbolic regression but also in other data-driven scientific fields, such as the data-driven PDE discover, ODE discover Long et al. (2019); Hu et al. (2022); Xu et al. (2023a); North et al. (2023), stability prediction Ghadami and Epureanu (2022); Alfarano et al. (2024) and numerical simulation Montáns et al. (2019); Kou and Zhang (2021); Alves and Fiuza (2022), contributing to advancements in chemistry, physics, biology, remote sensing, astronomy and many fields of engineering.

Acknowledgments

This work was partially supported by Major Program of National Natural Science Foundation of China (Nos.12292980, 12292984, 12031016, 12201024), National Key R&D Program of China (Nos.2023YFA1009000, 2023YFA1009004, 2020YFA0712203, 2020YFA0712201) and Beijing Natural Science Foundation (BNSF-Z210003).

References

- Alexey, D., 2020. An image is worth 16x16 words: Transformers for image recognition at scale. arXiv preprint arXiv:2010.11929 .
- Alfarano, A., Charton, F., Hayat, A., 2024. Global Lyapunov functions: a long-standing open problem in mathematics, with symbolic transformers. arXiv preprint arXiv:2410.08304 .
- Alves, E.P., Fiuza, F., 2022. Data-driven discovery of reduced plasma physics models from fully kinetic simulations. *Physical Review Research* 4, 033192.
- Antol, S., Agrawal, A., Lu, J., Mitchell, M., Batra, D., Zitnick, C.L., Parikh, D., 2015. Vqa: Visual question answering, in: *Proceedings of the IEEE international conference on computer vision*, pp. 2425–2433.
- Arnaldo, I., Krawiec, K., O'Reilly, U.M., 2014. Multiple regression genetic programming, in: *Proceedings of the 2014 Annual Conference on Genetic and Evolutionary Computation*, pp. 879–886.
- Asuncion, A., 2007. Uci machine learning repository, university of california, irvine, school of information and computer sciences. <http://www.ics.uci.edu/~mlern/MLRepository.html> .
- Baltrušaitis, T., Ahuja, C., Morency, L.P., 2018. Multimodal machine learning: A survey and taxonomy. *IEEE transactions on pattern analysis and machine intelligence* 41, 423–443.
- Biggio, L., Bendinelli, T., Neitz, A., Lucchi, A., Parascandolo, G., 2021. Neural symbolic regression that scales, in: *International Conference on Machine Learning*, Pmlr. pp. 936–945.
- Burlacu, B., Kommenda, M., Kronberger, G., Winkler, S.M., Affenzeller, M., 2023. Symbolic regression in materials science: Discovering interatomic potentials from data, in: *Genetic Programming Theory and Practice XIX*. Springer, pp. 1–30.
- Burlacu, B., Kronberger, G., Kommenda, M., 2020. Operon c++ an efficient genetic programming framework for symbolic regression, in: *Proceedings of the 2020 Genetic and Evolutionary Computation Conference Companion*, pp. 1562–1570.
- Cava, W.L., Singh, T.R., Taggart, J., Suri, S., Moore, J.H., 2018. Learning concise representations for regression by evolving networks of trees .
- Chang, H., Zhang, H., Barber, J., Maschinot, A., Lezama, J., Jiang, L., Yang, M.H., Murphy, K., Freeman, W.T., Rubinstein, M., et al., 2023. Muse: Text-to-image generation via masked generative transformers. arXiv preprint arXiv:2301.00704 .
- Cranmer, M., 2023. Interpretable machine learning for science with pysr and symbolicregression. jl. arXiv preprint arXiv:2305.01582 .
- Derner, E., Kubalík, J., Babuška, R., 2018. Data-driven construction of symbolic process models for reinforcement learning, in: *2018 IEEE International Conference on Robotics and Automation (ICRA)*, IEEE. pp. 5105–5112.
- Feynman, R.P., Leighton, R.B., Sands, M., 2015. *The Feynman lectures on physics, Vol. I: The new millennium edition: mainly mechanics, radiation, and heat. volume 1. Basic books.*
- de Franca, F.O., Aldeia, G.S.I., 2021. Interaction–transformation evolutionary algorithm for symbolic regression. *Evolutionary computation* 29, 367–390.
- Frome, A., Corrado, G.S., Shlens, J., Bengio, S., Dean, J., Ranzato, M., Mikolov, T., 2013. Devise: A deep visual-semantic embedding model. *Advances in neural information processing systems* 26.
- Gandhi, A., Adhvaryu, K., Poria, S., Cambria, E., Hussain, A., 2023. Multimodal sentiment analysis: A systematic review of history, datasets, multimodal fusion methods, applications, challenges and future directions. *Information Fusion* 91, 424–444.
- Ghadami, A., Epureanu, B.I., 2022. Data-driven prediction in dynamical systems: recent developments. *Philosophical Transactions of the Royal Society A* 380, 20210213.
- Gutmann, M., Hyvärinen, A., 2010. Noise-contrastive estimation: A new estimation principle for unnormalized statistical models, in: *Proceedings of the thirteenth international conference on artificial intelligence and statistics, JMLR Workshop and Conference Proceedings*. pp. 297–304.
- Han, J., Gong, K., Zhang, Y., Wang, J., Zhang, K., Lin, D., Qiao, Y., Gao, P., Yue, X., 2024. Onellm: One framework to align all modalities with language, in: *Proceedings of the IEEE/CVF Conference on Computer Vision and Pattern Recognition*, pp. 26584–26595.
- He, K., Zhang, X., Ren, S., Sun, J., 2016. Deep residual learning for image recognition, in: *Proceedings of the IEEE conference on computer vision and pattern recognition*, pp. 770–778.
- Hu, P., Yang, W., Zhu, Y., Hong, L., 2022. Revealing hidden dynamics from time-series data by odenet. *Journal of Computational Physics* 461, 111203.
- Jia, C., Yang, Y., Xia, Y., Chen, Y.T., Parekh, Z., Pham, H., Le, Q., Sung, Y.H., Li, Z., Duerig, T., 2021. Scaling up visual and vision-language representation learning with noisy text supervision, in: *International conference on machine learning*, PMLR. pp. 4904–4916.
- Jin, Y., Fu, W., Kang, J., Guo, J., Guo, J., 2019. Bayesian symbolic regression. arXiv preprint arXiv:1910.08892 .
- Jordan, M.I., Mitchell, T.M., 2015. *Machine learning: Trends, perspectives, and prospects*. *Science* 349, 255–260.

- Kamienny, P.A., d'Ascoli, S., Lample, G., Charton, F., 2022. End-to-end symbolic regression with transformers. *Advances in Neural Information Processing Systems* 35, 10269–10281.
- Kim, S., Lu, P.Y., Mukherjee, S., Gilbert, M., Jing, L., Čeperić, V., Soljačić, M., 2020. Integration of neural network-based symbolic regression in deep learning for scientific discovery. *IEEE transactions on neural networks and learning systems* 32, 4166–4177.
- Kou, J., Zhang, W., 2021. Data-driven modeling for unsteady aerodynamics and aeroelasticity. *Progress in Aerospace Sciences* 125, 100725.
- Koza, J.R., 1993. Genetic programming: On the programming of computers by means of natural selection (complex adaptive systems). A Bradford Book 1, 18.
- Krenn, M., Pollice, R., Guo, S.Y., Aldeghi, M., Cervera-Lierta, A., Friederich, P., dos Passos Gomes, G., Häse, F., Jinich, A., Nigam, A., et al., 2022. On scientific understanding with artificial intelligence. *Nature Reviews Physics* 4, 761–769.
- La Cava, W., Orzechowski, P., Burlacu, B., de França, F.O., Virgolin, M., Jin, Y., Kommenda, M., Moore, J.H., 2021. Contemporary symbolic regression methods and their relative performance. *arXiv preprint arXiv:2107.14351*.
- La Cava, W., Singh, T.R., Taggart, J., Suri, S., Moore, J.H., 2018. Learning concise representations for regression by evolving networks of trees. *arXiv preprint arXiv:1807.00981*.
- La Cava, W., Spector, L., Danai, K., 2016. Epsilon-lexicase selection for regression, in: *Proceedings of the Genetic and Evolutionary Computation Conference 2016*, pp. 741–748.
- Landajuela, M., Lee, C.S., Yang, J., Glatt, R., Santiago, C.P., Aravena, I., Mundhenk, T., Mulcahy, G., Petersen, B.K., 2022. A unified framework for deep symbolic regression. *Advances in Neural Information Processing Systems* 35, 33985–33998.
- Lee, J., Lee, Y., Kim, J., Kosiorek, A., Choi, S., Teh, Y.W., 2019. Set transformer: A framework for attention-based permutation-invariant neural networks, in: *International conference on machine learning*, PMLR. pp. 3744–3753.
- Li, J., Selvaraju, R., Gotmare, A., Joty, S., Xiong, C., Hoi, S.C.H., 2021. Align before fuse: Vision and language representation learning with momentum distillation. *Advances in neural information processing systems* 34, 9694–9705.
- Li, L., Tayir, T., Han, Y., Tao, X., Velásquez, J.D., 2023. Multimodality information fusion for automated machine translation. *Information Fusion* 91, 352–363.
- Li, Y., Li, W., Yu, L., Wu, M., Liu, J., Li, W., Hao, M., Wei, S., Deng, Y., 2024a. Discovering mathematical formulas from data via gpt-guided monte carlo tree search. *arXiv preprint arXiv:2401.14424*.
- Li, Y., Li, W., Yu, L., Wu, M., Liu, J., Li, W., Hao, M., Wei, S., Deng, Y., 2024b. Generative pre-trained transformer for symbolic regression base in-context reinforcement learning. *arXiv preprint arXiv:2404.06330*.
- Li, Y., Li, W., Yu, L., Wu, M., Liu, J., Li, W., Wei, S., Deng, Y., 2024c. Mllm-sr: Conversational symbolic regression base multi-modal large language models. *arXiv preprint arXiv:2406.05410*.
- Li, Y., Liu, J., Wu, M., Yu, L., Li, W., Ning, X., Li, W., Hao, M., Deng, Y., Wei, S., 2025. Mmsr: Symbolic regression is a multi-modal information fusion task. *Information Fusion* 114, 102681.
- Li, Y., Panda, R., Kim, Y., Chen, C.F.R., Feris, R.S., Cox, D., Vasconcelos, N., 2022. Valhalla: Visual hallucination for machine translation, in: *Proceedings of the IEEE/CVF Conference on Computer Vision and Pattern Recognition*, pp. 5216–5226.
- Lin, H., Meng, F., Su, J., Yin, Y., Yang, Z., Ge, Y., Zhou, J., Luo, J., 2020. Dynamic context-guided capsule network for multimodal machine translation, in: *Proceedings of the 28th ACM international conference on multimedia*, pp. 1320–1329.
- Liu, J., Li, W., Yu, L., Wu, M., Sun, L., Li, W., Li, Y., 2023. Snr: Symbolic network-based rectifiable learning framework for symbolic regression. *Neural Networks* 165, 1021–1034.
- Liu, J., Wu, M., Yu, L., Li, W., Li, W., Li, Y., Hao, M., Deng, Y., Shu, W., 2024. Camo: Capturing the modularity by end-to-end models for symbolic regression. *Knowledge-Based Systems*, 112747.
- Liu, X., Zhao, J., Sun, S., Liu, H., Yang, H., 2021. Variational multimodal machine translation with underlying semantic alignment. *Information Fusion* 69, 73–80.
- Long, Z., Lu, Y., Dong, B., 2019. Pde-net 2.0: Learning pdes from data with a numeric-symbolic hybrid deep network. *Journal of Computational Physics* 399, 108925.
- Lu, J., Batra, D., Parikh, D., Lee, S., 2019. Vilbert: Pretraining task-agnostic visiolinguistic representations for vision-and-language tasks. *Advances in neural information processing systems* 32.
- Lu, Y., Wu, Y., Liu, B., Zhang, T., Li, B., Chu, Q., Yu, N., 2020. Cross-modality person re-identification with shared-specific feature transfer, in: *Proceedings of the IEEE/CVF conference on computer vision and pattern recognition*, pp. 13379–13389.
- Mahesh, B., 2020. Machine learning algorithms-a review. *International Journal of Science and Research (IJSR)*. [Internet] 9, 381–386.
- Matsubara, Y., Chiba, N., Igarashi, R., Ushiku, Y., 2022. Rethinking symbolic regression datasets and benchmarks for scientific discovery. *arXiv preprint arXiv:2206.10540*.
- McConaghy, T., 2011. Ffx: Fast, scalable, deterministic symbolic regression technology. *Genetic Programming Theory*

- and Practice IX , 235–260.
- Merler, M., Dainese, N., Haitsiukevich, K., 2024. In-context symbolic regression: Leveraging language models for function discovery. arXiv preprint arXiv:2404.19094 .
- Meurer, A., Smith, C.P., Paprocki, M., Čertík, O., Kirpichev, S.B., Rocklin, M., Kumar, A., Ivanov, S., Moore, J.K., Singh, S., et al., 2017. Sympy: symbolické výpočty v pythonu .
- Montáns, F.J., Chinesta, F., Gómez-Bombarelli, R., Kutz, J.N., 2019. Data-driven modeling and learning in science and engineering. *Comptes Rendus Mécanique* 347, 845–855.
- Mundhenk, T.N., Landajuela, M., Glatt, R., Santiago, C.P., Faissol, D.M., Petersen, B.K., 2021. Symbolic regression via neural-guided genetic programming population seeding. arXiv preprint arXiv:2111.00053 .
- Neumann, P., Cao, L., Russo, D., Vassiliadis, V.S., Lapkin, A.A., 2020. A new formulation for symbolic regression to identify physico-chemical laws from experimental data. *Chemical Engineering Journal* 387, 123412.
- Ngiam, J., Khosla, A., Kim, M., Nam, J., Lee, H., Ng, A.Y., 2011. Multimodal deep learning, in: Proceedings of the 28th international conference on machine learning (ICML-11), pp. 689–696.
- North, J.S., Wikle, C.K., Schliep, E.M., 2023. A review of data-driven discovery for dynamic systems. *International Statistical Review* 91, 464–492.
- Petersen, B.K., Landajuela, M., Mundhenk, T.N., Santiago, C.P., Kim, S.K., Kim, J.T., 2019. Deep symbolic regression: Recovering mathematical expressions from data via risk-seeking policy gradients. arXiv preprint arXiv:1912.04871 .
- Poincaré, H., Frappier, M., Stump, D.J., 2017. Science and hypothesis .
- Quade, M., Abel, M., Shafí, K., Niven, R.K., Noack, B.R., 2016. Prediction of dynamical systems by symbolic regression. *Physical Review E* 94, 012214.
- Radford, A., Kim, J.W., Hallacy, C., Ramesh, A., Goh, G., Agarwal, S., Sastry, G., Askell, A., Mishkin, P., Clark, J., et al., 2021. Learning transferable visual models from natural language supervision, in: International conference on machine learning, PMLR. pp. 8748–8763.
- Ramanishka, V., Das, A., Park, D.H., Venugopalan, S., Hendricks, L.A., Rohrbach, M., Saenko, K., 2016. Multimodal video description, in: Proceedings of the 24th ACM international conference on Multimedia, pp. 1092–1096.
- Ramesh, A., Pavlov, M., Goh, G., Gray, S., Voss, C., Radford, A., Chen, M., Sutskever, I., 2021. Zero-shot text-to-image generation, in: International conference on machine learning, Pmlr. pp. 8821–8831.
- Saharia, C., Chan, W., Saxena, S., Li, L., Whang, J., Denton, E.L., Ghasemipour, K., Gontijo Lopes, R., Karagol Ayan, B., Salimans, T., et al., 2022. Photorealistic text-to-image diffusion models with deep language understanding. *Advances in neural information processing systems* 35, 36479–36494.
- Sahoo, S., Lampert, C., Martius, G., 2018. Learning equations for extrapolation and control, in: International Conference on Machine Learning, Pmlr. pp. 4442–4450.
- Schmidt, M., Lipson, H., 2009. Distilling free-form natural laws from experimental data. *science* 324, 81–85.
- Schmidt, M.D., Lipson, H., 2010. Age-fitness pareto optimization, in: Proceedings of the 12th annual conference on Genetic and evolutionary computation, pp. 543–544.
- Shen, J., Li, L., Dery, L.M., Staten, C., Khodak, M., Neubig, G., Talwalkar, A., 2023. Cross-modal fine-tuning: Align then refine, in: International Conference on Machine Learning, PMLR. pp. 31030–31056.
- Shojaee, P., Meidani, K., Barati Farimani, A., Reddy, C., 2023. Transformer-based planning for symbolic regression. *Advances in Neural Information Processing Systems* 36, 45907–45919.
- Shojaee, P., Meidani, K., Barati Farimani, A., Reddy, C., 2024. Transformer-based planning for symbolic regression. *Advances in Neural Information Processing Systems* 36.
- Strogatz, S.H., 2018. Nonlinear dynamics and chaos: with applications to physics, biology, chemistry, and engineering. CRC press.
- Surden, H., 2021. Machine learning and law: An overview. *Research Handbook on Big Data Law* , 171–184.
- Szegedy, C., Liu, W., Jia, Y., Sermanet, P., Reed, S., Anguelov, D., Erhan, D., Vanhoucke, V., Rabinovich, A., 2015. Going deeper with convolutions, in: Proceedings of the IEEE conference on computer vision and pattern recognition, pp. 1–9.
- Tan, H., Bansal, M., 2019. Lxmert: Learning cross-modality encoder representations from transformers. arXiv preprint arXiv:1908.07490 .
- Udrescu, S.M., Tan, A., Feng, J., Neto, O., Wu, T., Tegmark, M., 2020. Ai feynman 2.0: Pareto-optimal symbolic regression exploiting graph modularity. *Advances in Neural Information Processing Systems* 33, 4860–4871.
- Valipour, M., You, B., Panju, M., Ghodsi, A., 2021. Symbolicgpt: A generative transformer model for symbolic regression. arXiv preprint arXiv:2106.14131 .
- Van Den Oord, A., Vinyals, O., et al., 2017. Neural discrete representation learning. *Advances in neural information processing systems* 30.
- Vanschoren, J., Van Rijn, J.N., Bischl, B., Torgo, L., 2014. Openml: networked science in machine learning. *ACM SIGKDD Explorations Newsletter* 15, 49–60.
- Vastl, M., Kulhánek, J., Kubalík, J., Dermer, E., Babuška, R., 2024. Symformer: End-to-end symbolic regression using transformer-based architecture. *IEEE Access* .
- Virgolin, M., Alderliesten, T., Bosman, P.A., 2019. Linear scaling with and within semantic backpropagation-based

- genetic programming for symbolic regression, in: Proceedings of the genetic and evolutionary computation conference, pp. 1084–1092.
- Virgolin, M., Alderliesten, T., Witteveen, C., Bosman, P.A., 2017. Scalable genetic programming by gene-pool optimal mixing and input-space entropy-based building-block learning, in: Proceedings of the Genetic and Evolutionary Computation Conference, pp. 1041–1048.
- Wang, H., Fu, T., Du, Y., Gao, W., Huang, K., Liu, Z., Chandak, P., Liu, S., Van Katwyk, P., Deac, A., et al., 2023. Scientific discovery in the age of artificial intelligence. *Nature* 620, 47–60.
- Xu, H., Zeng, J., Zhang, D., 2023a. Discovery of partial differential equations from highly noisy and sparse data with physics-informed information criterion. *Research* 6, 0147.
- Xu, Y., Liu, Y., Sun, H., 2023b. Rsrn: Reinforcement symbolic regression machine. arXiv preprint arXiv:2305.14656 .
- Yao, S., Wan, X., 2020. Multimodal transformer for multimodal machine translation, in: Proceedings of the 58th annual meeting of the association for computational linguistics, pp. 4346–4350.
- Yin, T., Zhou, X., Krähenbühl, P., 2021. Multimodal virtual point 3d detection. *Advances in Neural Information Processing Systems* 34, 16494–16507.
- Yin, Y., Meng, F., Su, J., Zhou, C., Yang, Z., Zhou, J., Luo, J., 2020. A novel graph-based multi-modal fusion encoder for neural machine translation. arXiv preprint arXiv:2007.08742 .
- Zhang, Z., Chen, K., Wang, R., Utiyama, M., Sumita, E., Li, Z., Zhao, H., 2020. Neural machine translation with universal visual representation, in: International Conference on Learning Representations.
- Zhong, G., Wang, L.N., Ling, X., Dong, J., 2016. An overview on data representation learning: From traditional feature learning to recent deep learning. *The Journal of Finance and Data Science* 2, 265–278.
- Zhu, L., Zhu, Z., Zhang, C., Xu, Y., Kong, X., 2023. Multimodal sentiment analysis based on fusion methods: A survey. *Information Fusion* 95, 306–325.

Appendix A. Data generation

ViSymRe and other pre-trained models are trained and tested on a pre-generated dataset, in which each sample is considered as a combination: a support point set and an equation image (only used by ViSymRe) as input, and an equation skeleton as target. Note that the sampling of support points and the visualization of equations are synchronously performed during training and testing based on the equation skeleton, so in fact the pre-generated dataset only contains equation skeletons. The details about equation skeletons generation, support point sampling and visualization are introduced below.

Appendix A.1. Equation skeleton generator

The method we employ for generating mathematical equation skeleton is improved from the open source code provided by Biggio et al. (2021). In this approach, equation is conceptualized as a binary tree. The non-leaf nodes represent operators. The leaf nodes are reserved for the variables or constants.

For the leaf nodes, which represent either variables or constants, we set a probabilistic framework for their selection:

- The probability of a leaf node being a variable is set at 0.8.
- The probability of a leaf node being an constant is set at 0.2. Furthermore, the probability of being a general constant is 0.8, and the probability of being a special constant (such as π and e) is 0.2.

For multivariable equations, there are constraints regarding the inclusion of variables:

- If the variable x_2 is present in a tree, x_1 must also be included.
- Similarly, if x_3 is included, both x_1 and x_2 must be present.

Additionally, we employ a strategy same as that of the decoder described in Section 3.4 to avoid meaningless nesting. After the trees are constructed, we perform traversal to transform them into semantically equivalent strings using the pre-order representation. Finally, we simplify them using the Sympy library in Python Meurer et al. (2017), and the constants in the simplified equations are replaced with the placeholder 'c' to obtain the skeletons.

In Table A.3, we present the comprehensive parameters employed by our equation skeleton generator. Note that, although the constants are initially sampled from the $\mathcal{U}(0, 10)$, they form a broader distribution after undergoing internal operations during the simplifying. The same applies to the exponents.

Fig. A.13 presents the statistical data of 1000 equation skeletons generated by the proposed equation skeleton generator, including equation complexity, the number of equations with different numbers of variables, the proportion of equations with different unary operators, and the total occurrences of different unary operators. On the whole, the statistical data adheres to the basic assumptions of equation distribution: the number of equations decreases with the increase in variables, the complexity of equations and the rarity of unary operators.

Table A.3: The parameters employed by equation generator.

Description	Value
Max number of variables	3 (for in-domain experiments) or 10 (for out-of-domain experiments)
Max number of unary operators	$Max(5, Number(variables))$
Max number of binary operators	$Max(10, 2 \times Number(variables))$
Max number of constants	5
Max number of nodes	50
Distribute of exponents	$\{-5, -3, -2, -1, 1, 2, 3, 5\}$
Distribute of constants	$\mathcal{U}(0, 10)$
Frequency of binary operators	add:1, div:1, mul:1, sub:1
Frequency of unary operators	abs:1, pow2:3, pow3:2, pow5:1, sqrt:1, sin:1, cos:1, tan:0.2, arcsin:0.2, log:0.2, exp:1
Min number of support points	100
Max number of support points	300

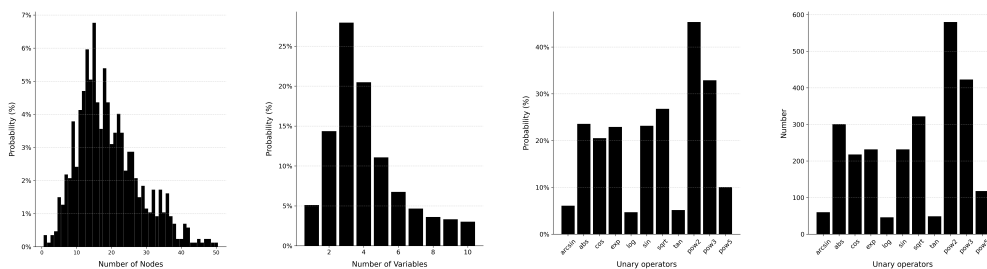


Figure A.13: Statistical data of 1000 equation skeletons.

Appendix A.2. Support points sampling

For each equation skeleton, we first sample constants following the distribution in Table A.3, and then sample n points for each variable. To enhance the diversity of sample distributions, we divide n points into k clusters ($k \sim \mathcal{U}\{1, k_{max}\}$ with k_{max} is generally 5) Kamienny et al. (2022). Points within each cluster are sampled from a Uniform distribution whose maximum and minimum values are randomly determined. The minimum values follow an exponential distribution (with $\lambda = 1/2$), and the difference between the maximum and minimum values is distributed according to a normal distribution ($\mathcal{N}(5, 5)$). Fig A.14 shows the histograms of the minimum and maximum values. For each cluster, 30% of the points are randomly selected to be negative. After the points of all variables are sampled, they are substituted into the equation to calculate the target. A complete set of support points is formatted as $D = \{(x_1, \dots, x_d, y_i)\}_{i=1}^n \in \mathbb{R}^{n \times (d+1)}$. When the model is designed to support more than d variables, the points of remaining variables are padded with 0s.

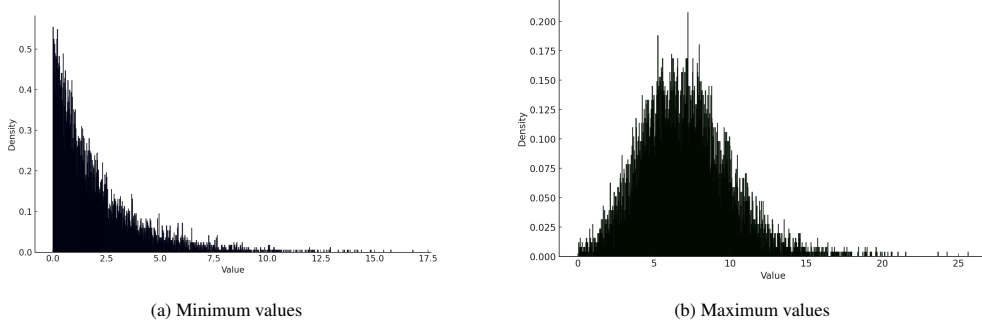


Figure A.14: Distribution histogram of minimum and maximum values that determine the support points distribution.

Appendix A.3. Visual generation

Generally, for an equation involving d variables, we iteratively apply Algorithms 1 and 2 d times, $x_i, i = 1, 2, \dots, d$ as the retention variable in the i -th iteration, with the processed equation denoted as f_i . We randomly sample 200 points from the range $[-10, 10]$ to visualize the $(x_i, f_i(x_i))$. Then use the grayscale technology to convert the image to a single channel, and use binarization (0 or 1) to make the curves clear. Finally, all images about d variables are reshaped and stacked along the channel dimension, resulting in a composite image of dimensions $64 \times 64 \times d$, which serves as the visual representation of the equation. When the model is designed to support more than d variables, the remaining channels are padded with 0s.

Appendix A.4. Lookup table generation

The required lookup table is built synchronously during the training, without additional manual annotation. Specifically, we save the image locally and name it with the equation skeleton (the hash value) to establish the image-skeleton correspondence. If it is a multivariable equation, each channel is saved separately. When training a new equation, first search for its corresponding image in the lookup table. If it does not exist, the lookup table is updated. Note that, the lookup table is only useful during the training, because neither the equation nor the equation image is available during the inference.

Appendix B. Additional in-domain experiments

Table B.4 reports a set of equations correctly predicted by ViSymRe but incorrectly by NeSymReS and SymbolicGPT. Analysis shows that the baselines inadequately learn the special constants and unary operators, resulting in some equations containing these symbols not being correctly predicted, thus generating more complex equations to fit the data. In contrast, ViSymRe potentially emphasizes unary operators in the process of visualization, as their visual features, such as wavy lines and arcs, are highly prominent, while retaining the impact of special constants on visualization. This enables ViSymRe to effectively learn the features of these symbols with the support of visual information.

Fig. B.15 presents some examples, comparing the real equation images with those reconstructed from support points by ViSymRe. In most cases, ViSymRe can successfully reconstruct the equation images. Although the resolution of all reconstructed images is maintained at a low

Table B.4: A set of equations that are correctly predicted by ViSymRe but incorrectly predicted by baselines. “~” indicate prediction failure.

Real	ViSymRe	NeSymReS	SymbolicGPT
$x_1 + \frac{\sin(x_2)}{x_1^2 x_2}$	$x_1 + \frac{\sin(1.001 \cdot x_2)}{x_1^2 \cdot x_2}$	$x_1 - \frac{\tan(1.6 \cdot x_2)}{2 \cdot x_1^2 \cdot x_2}$	$x_1 + 0.007 \cdot \frac{x_2}{x_1^2 \cdot (17.805 \cdot x_1 + x_2 - 4.786)}$
$\sin(\pi \cdot x_1^2 \cdot x_2)$	$\sin(\pi \cdot x_1^2 \cdot x_2)$	$\sin(x_1^2 \cdot (x_2 + 1.116))$	~
$x_1 \cdot (\sqrt{x_2} + x_3)$	$x_1 \cdot (\sqrt{x_2} + x_3)$	$x_1 \cdot \left(\frac{x_2}{x_1 + 0.274} + x_3\right) + x_1$	$x_1 \cdot (x_3 + \ln(x_1 + x_2^2))$
$(x_1^2 - x_2 \cdot x_3)^2$	$(x_1^2 - x_2 \cdot x_3)^2$	$x_2 \cdot x_3 + 78.897 \cdot (x_1 - 0.692 \cdot x_2)^2$	$80.691 \cdot (x_1 - 0.126 \cdot x_2 \cdot x_3)^2$
$x_1 \cdot (x_1 + x_2) \cdot \exp(-x_3)$	$x_1 \cdot ((x_1 + x_2) \cdot \exp(-x_3))$	$\frac{730832.475 \cdot x_1 \cdot \exp(-x_3)}{x_2 + 260246.065 \cdot x_3}$	$\frac{x_1 \cdot (x_1 + x_2 \cdot (x_1 - 0.5160))}{(x_2 + x_3) \cdot (x_3 + 0.534)}$
$\frac{x_1 \cdot x_2}{x_3 - e}$	$\frac{x_1 \cdot x_2}{x_3 - e}$	$\frac{x_1 - 4.56}{1.1482 \cdot x_2 - \pi}$	$\frac{x_1 - 2.933}{-0.247 \cdot x_1 + 2 \cdot x_2 - \pi}$
$x_1 \cdot (\sqrt{x_2} + \exp(2))$	$x_1 \cdot (x_2^{0.5} + 7.38)$	$4.068 \cdot x_1 \cdot \ln(30.353 \cdot x_2 + \pi + 79.483)$	$8.251 \cdot x_1 \cdot \ln(-0.033 \cdot x_1 + x_2 + 9.703)$
$\frac{\ln(x_1)}{x_2 - e}$	$((x_2 - e)^{-1} \cdot \ln(x_1))$	$\frac{x_1 - 6.045}{-x_1 + 5.701 \cdot x_2 - 6.0738}$	~
$x_1 + x_2 - \sin(\sqrt{x_1 \cdot x_3})$	$x_1 + (x_2 - \sin(\sqrt{x_1 \cdot x_3}))$	~	$x_1 + x_2 - \cos\left(\frac{x_3}{x_2 - 0.887}\right) + 0.352$
$-x_1^2 + \cos(x_1^2)$	$-x_1^2 + \cos(x_1^2)$	$-x_1^2 - 0.002 \cdot x_1 + 0.048$	$-x_1^2 - 0.063 \cdot x_1 + 0.351$
$x_2 \cdot x_3 \cdot \left(x_1 + x_2 + \sin\left(\frac{x_1}{x_3}\right)\right)$	$x_2 \cdot x_3 \cdot \left(x_1 + x_2 + \sin\left(\frac{x_1}{x_3}\right)\right)$	$1.079 \cdot x_2 \cdot x_3 \cdot (x_1 + 0.925 \cdot x_2 + 0.153)$	$x_2 \cdot x_3 \cdot (1.083 \cdot x_1 + x_2 + 0.139)$

dimension of 64×64 , which limits the display of some details such as the rapidly changing curves of trigonometric functions, the basic outlines and structures are well preserved. This capability indicates that ViSymRe adapts well to capturing essential visual information from the support points sampled from equations with varying variables and complexities, thereby providing valid assistance for further mechanism analysis and equation prediction.

Appendix C. Details of the used databases

Feynman database: The Feynman database comes from first principles models of physical systems, representing the static systems. It contains 119 symbolic regression problems from the Feynman Lectures on Physics Feynman et al. (2015), which are recently compiled into datasets that serve as a benchmark for evaluating symbolic regression models Udrescu et al. (2020).

ODE-Strogatz database: The ODE-Strogatz database Strogatz (2018) also comes from first principles models of physical systems, representing the non-linear and chaotic dynamical processes. It comprises 14 problems, each detailing the trajectory of a 2-state system governed by a first-order ordinary differential equation (ODE).

Black box regression database: The black box regression problems originate from various open-source repositories, such as OpenML Vanschoren et al. (2014) and the UCI repository Asuncion (2007). They comprise 46 “real-world” problems (collected from true physical processes) and 76 synthetic problems (generated from static equations or simulations).

SRSD-Feynman database: SRSD-Feynman Matsubara et al. (2022) is an improved benchmark of Feynman database (FSRD) Udrescu et al. (2020). Here are the key distinctions of them:

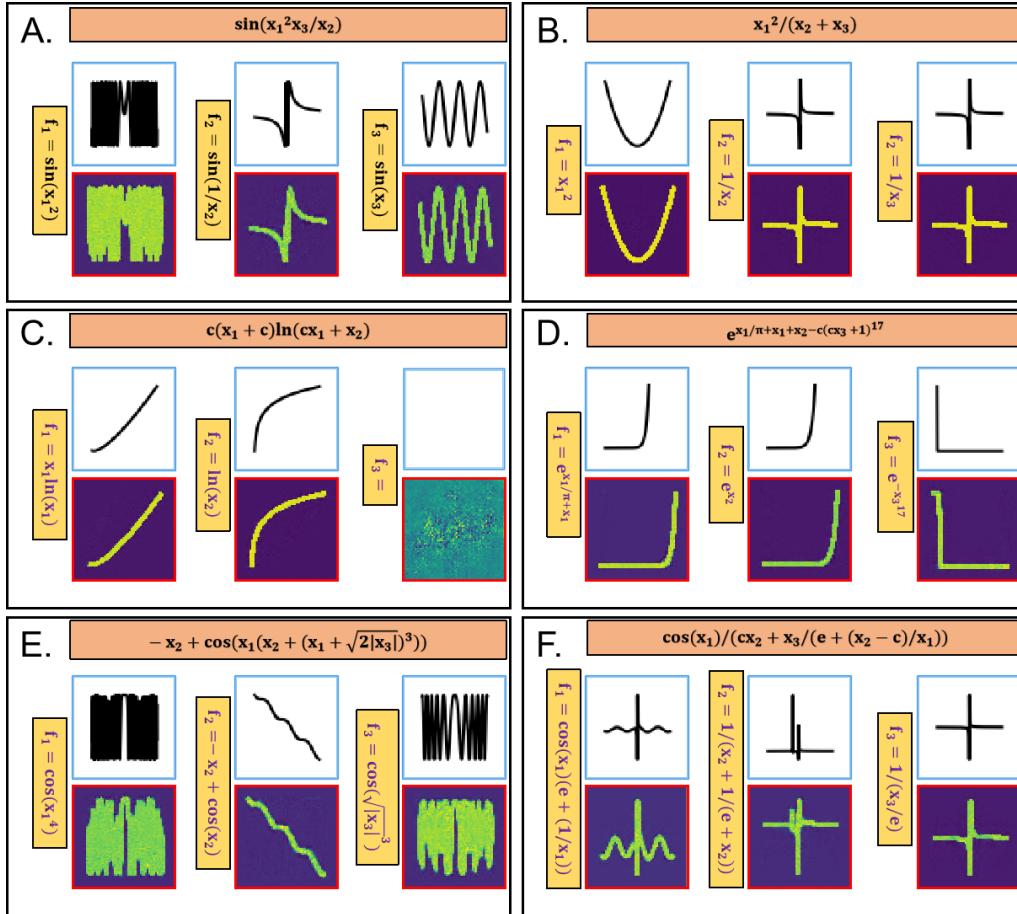


Figure B.15: **Typical images reconstructed by ViSymRe from support points.** Each block represents an instance, with the orange box enclosing the original equation skeleton, the yellow box enclosing the preprocessed equation, the blue box enclosing the real image and the red box enclosing the reconstructed image. Each instance represents a typical type of equation: trigonometric equations (A), polynomial equations (B), logarithmic equations (C), rapidly growing exponential equations (D), absolute value equations (E) and equations containing special constants (F).

- In SRSD, physical constants such as the speed of light and gravitational are treated as true constants, whereas in FSRD, they are treated as variables.
- Some duplicate problems in FSRD have identical equation and sampling range, which are addressed in SRSD by treating them as separate problems.
- SRSD defines sampling ranges based on typical physics experiments, using SI units that are more appropriate for confirming physical phenomena.

Appendix D. Additional pseudo-codes

Algorithm 3 is used to monitor the ancestor nodes of the current position in the decoding process, to limit the structure of the outputted equations. This algorithm has the potential to capture more information from the ancestor nodes, such as units and frequencies, to further promote dimensional consistency of the output equations, which we will consider in future work.

Algorithm 3 Ancestor nodes search algorithm

```

1: Input:  $\mathcal{T}$  : Current equation tree
2: Output:  $\mathcal{N}$  : Ancestor nodes
3: function SEARCH_ANCESTOR_NODES( $\mathcal{T}$ )
4:    $\mathcal{N} \leftarrow []$  // Store ancestor nodes
5:   child_counter  $\leftarrow []$  // Track the number of child nodes
6:   for node  $\in \mathcal{T}$  do // Traverse the nodes in the tree
7:     if node  $\in$  Unary Operators then
8:        $\mathcal{N} \leftarrow \mathcal{N} \cup$  node
9:       child_counter  $\leftarrow$  child_counter  $\cup$  1 // Add 1 to child_counter for unary operations
10:    else if node  $\in$  Binary Operators then
11:       $\mathcal{N} \leftarrow \mathcal{N} \cup$  node
12:      child_counter  $\leftarrow$  child_counter  $\cup$  2 // Add 2 to child_counter for binary
operations
13:    else if node  $\in$  Variable or node  $\in$  Constant then
14:      if child_counter  $\neq \emptyset$  then
15:        child_counter[-1]  $\leftarrow$  child_counter[-1] - 1 // Subtract 1 to child_counter for
variable and constant
16:      end if
17:    end if
18:    while child_counter  $\neq \emptyset$  and child_counter[-1] = 0 do
19:       $\mathcal{N} \leftarrow \mathcal{N} \setminus \mathcal{N}[-1]$ 
20:      child_counter  $\leftarrow$  child_counter  $\setminus$  child_counter[-1]
21:      child_counter[-1]  $\leftarrow$  child_counter[-1] - 1
22:    end while
23:  end for
24:  return  $\mathcal{N}$  // Return the ancestor nodes of the current position
25: end function
26:  $\mathcal{N} \leftarrow$  SEARCH_ANCESTOR_NODES( $\mathcal{T}$ )

```
